



LAWRENCE
LIVERMORE
NATIONAL
LABORATORY

Effect of Initial Conditions on 2D Rayleigh-Taylor Instability and Transition to Turbulence in Planar Blast-wave-driven Systems

A. R. Miles, M. J. Edwards, J. A. Greenough

March 31, 2004

Physics of Plasmas

Disclaimer

This document was prepared as an account of work sponsored by an agency of the United States Government. Neither the United States Government nor the University of California nor any of their employees, makes any warranty, express or implied, or assumes any legal liability or responsibility for the accuracy, completeness, or usefulness of any information, apparatus, product, or process disclosed, or represents that its use would not infringe privately owned rights. Reference herein to any specific commercial product, process, or service by trade name, trademark, manufacturer, or otherwise, does not necessarily constitute or imply its endorsement, recommendation, or favoring by the United States Government or the University of California. The views and opinions of authors expressed herein do not necessarily state or reflect those of the United States Government or the University of California, and shall not be used for advertising or product endorsement purposes.

**Effect of Initial Conditions on 2D Rayleigh-Taylor
Instability and Transition to Turbulence in Planar
Blast-wave-driven Systems**

A. R. Miles^{1,2}, M. J. Edwards², J. A. Greenough²

¹Lawrence Livermore National Laboratory,

²University of Maryland at College Park

From a dissertation to be submitted to the Graduate School, University of Maryland, by
Aaron Miles in partial fulfillment of the requirements for the Ph.D. Degree in Physics.

Perturbations on an interface driven by a strong blast wave grow in time due to a
combination of Rayleigh-Taylor, Richtmyer-Meshkov, and decompression effects. In this
paper, we present the first results from a computational study of such a system under
drive conditions to be attainable on the National Ignition Facility. Using the multi-
physics, AMR, higher order Godunov Eulerian hydrocode, Raptor, we consider the late
nonlinear instability evolution for multiple amplitude and phase realizations of a variety
of multimode spectral types. We show that compressibility effects preclude the

emergence of a regime of self-similar instability growth independent of the initial conditions by allowing for memory of the initial conditions to be retained in the mix-width at all times. The loss of transverse spectral information is demonstrated, however, along with the existence of a quasi-self-similar regime over short time intervals. Certain aspects of the initial conditions, including the rms amplitude, are shown to have a strong effect on the time to transition to the quasi-self-similar regime.

I. Introduction

The post-linear evolution of the Rayleigh-Taylor (RT) instability^{1,2} remains incompletely understood. This is particularly true for multimode perturbations, which are also the most important for practical applications in inertial confinement fusion (ICF) and astrophysics. There is some evidence from theoretical,^{3,4} computational,⁵ and experimental⁶ work that memory of the initial perturbation spectrum is lost as the interface evolves into a self-similar regime in which the mix width grows in proportion with the dominant transverse scale length. The existence of such a regime has yet to be proven, however, even for the most fundamental case of incompressible fluids in a uniform gravitational field. In addition, many physical systems of interest involve compressible systems undergoing time-varying accelerations, where results obtained for the idealized case do not necessarily apply. One class of such systems includes core-collapse supernovae, in which strong blast waves propagate from near the star's core up

through layers of progressively less dense material.^{7,8} Each driven interface is susceptible to both RT and Richtmyer-Meshkov^{9,10} (RM) instabilities.¹¹ In addition, perturbation growth results from material expansion in the large-scale velocity gradient behind the shock front.^{12,13} Understanding the growth of the resulting turbulent mixing zone may be required to explain the anomalously-fast transport of core material to the star's surface.^{7,8,14,15}

In order to study this problem, a series of laser-driven laboratory experiments have been designed and conducted on the Nova¹⁶ and Omega¹⁷ lasers,^{12,13,18-25} and additional experiments are currently being planned for the National Ignition Facility²⁶ (NIF). These experiments are intended in part to study the effect of the initial conditions on the nonlinear instability growth, the time to transition, and growth of the post-transition turbulent mixing zone for high Mach number blast-wave driven systems. In this paper, we present computational results for a planer blast-wave-driven system under NIF-like drive conditions. Using the multi-physics, AMR, higher order Godunov Eulerian hydrocode, Raptor,²⁷ we consider the late nonlinear instability evolution for multiple amplitude and phase realizations of a variety of multimode spectral types. We show that compressibility leads to a breaking of the self-similarity and allows for memory of the initial conditions to be retained in the mix-width at all times. The loss of transverse spectral information is demonstrated, however, along with the existence of a quasi-self-similar regime over short time intervals. Aspects of the initial conditions, including the rms amplitude and characteristic wavelength, are shown to have a strong effect on the time to transition to the quasi-self-similar regime. Even different randomized amplitude

and phase realizations of the same initial spectrum develop significantly different late-time amplitudes and growth rates.

II. Code and calculation setup

The simulations are performed in 2D using the multi-physics radiation hydrodynamics code Raptor, which uses a 2nd order (in space and time) Godunov method applied to the Euler equations.²⁷ Raptor is parallelized and uses adaptive mesh refinement (AMR), making it well-suited to problems such as ours that require high resolution in only a portion of the computational domain. We use the LEOS equation of state (EOS) tables,²⁸ and include in the calculations electron conduction but not radiation.

Our hypothetical target (see schematic in Fig. 1a) represents an extension of previous and ongoing decelerating Rayleigh-Taylor experiments performed on the Omega laser and discussed in detail elsewhere.²⁵ The cylindrical target consists of a 150 μm plastic pusher section (density 1.42 g/cc) in contact with a less dense 2.2 mm payload section. An initial perturbation is machined onto the contact-surface end of the pusher. In place of the carbon foam payload used in the Omega experiments, we assume cryogenic hydrogen with density 0.086 g/cc. We expect that this change, which is motivated by uncertainties in the foam EOS tables,¹³ would not qualitatively change the results if carbon foam was to be used in the actual experiments.

The width the computational domain was typically 200 μm , so that the 50 μm wavelength in the previous 2D single-mode experiments corresponds to mode 4. The

typical resolution is 512 cells in the transverse direction (512 ppb), corresponding to 128 points per wavelength (ppw) in mode 4. Resolution finer and coarser by up to a factor of four in each direction was used in resolution studies that are detailed below. Open boundary conditions are used in the parallel (to the shock) direction while periodic conditions are specified in the transverse direction.

The end of the pusher opposite the perturbation is driven with a 1 ns laser pulse, which launches a strong blast wave into the target. We assume a pulse energy of 25 kJ for the NIF-like drive, which is five times greater than that used in the Omega experiments. This higher laser intensity would provide significant drive over a longer period of time than that achieved on previous experiments, and would allow for the generation of larger transverse scales. This is important in part because bubble-merger pictures of multimode instability evolution are generally thought to require multiple merger generations above the largest significant scales present in the initial conditions before a stationary scale-invariant bubble distribution is attained.⁵ A system is said to have progressed through one merger generation each time the characteristic transverse scale is doubled, so this corresponds to scales at least an order of magnitude larger than the initial conditions.

The simulations are initiated with a high-velocity, heated, compressed slab with characteristics taken from a laser-driven Lasnex²⁹ simulation at the end of the laser pulse.

The Mach numbers of the incident and transmitted blast waves are in the range of 10-30, where the precise value depends on the degree to which x-ray preheat can be controlled (the incident Mach number with no preheat would be about 60). The resulting initial interface speed is about 130 $\mu\text{m/ns}$ (see Fig. 1b). This is nearly twice the maximum interface speed obtained in the Omega experiments,¹³ and the instability is seen to

develop about twice as fast. The post-shock Atwood number remains nearly constant at about 0.7. The simulations are continued out to a maximum of 40 ns, which is about the latest time usable data has been obtained from the Omega experiments. Throughout the duration of the experiment, the interface is RT unstable due to the reversal there of the pressure and density gradients (typical pressure, density, and velocity profiles are shown in Fig. 2).

An estimate of the relative importance of RM to the instability growth is obtained from “pure RM” simulations driven by a steady shock with the same strength as that of the blast wave at the time it reaches the interface. In fig. 3, the growth rate from a pure RM calculation is compared to a blast-wave driven simulation. The same initial perturbation – large amplitude mode 4 with a narrow gaussian small amplitude short wavelength component (Fig. 4e and discussion below) – is used in both cases. The perturbation growth is dominated by RM for about the first ns, while combined RT plus decompression dominate at later times as the interface decelerates in the rarefaction behind the shock front. This is consistent with CALE simulations of Omega-driven systems in which the instability developed half as fast and RM was found to dominate for twice as long.¹³

III. Characterization of initial conditions

When we speak of dependence on initial conditions, we have in mind the effect of the initial perturbation spectrum on the observable properties of the mix region. During

the linear regime when mode coupling can be neglected, this can be determined in a straightforward manner from the linear (possibly time-dependent) growth rates. Well-established mode coupling models make the weakly nonlinear regime fairly tractable as well.³⁰⁻³² Our interest is the effect of the initial conditions on the instability growth in the strongly nonlinear regime; before, during, and after any transition to a self-similar or turbulent state.

The principle observables during the deep nonlinear phase are the amplitudes and growth rates of the spike and bubble fonts, and the statistical properties of the internal structure of the mix region. The internal structure of the interface region is characterized by spectra (density, kinetic energy, velocity, and enstrophy) and by the degree of small-scale mixing of the two fluids.

The most general distinction we make in classifying initial spectra is between continuous and bi-component spectra. Bi-component spectra include a long-wavelength component and a separated (in k -space) short-wavelength component. In this study, the long-wavelength component always consists of a single mode (mode 4) with a wavelength of $50\text{ }\mu\text{m}$ and initial amplitude that is typically $2.5\text{ }\mu\text{m}$. This is the same mode used in ongoing Omega experiments that we have previously modeled extensively.¹³ With its nominal initial amplitude, mode 4 is only marginally linear ($a/\lambda = 0.05$). The post-shock amplitude, however, is an order of magnitude smaller. The bi-component spectral class is particularly important for considering potential effects of short-wavelength “noise” – possibly unresolved in calculations or not included in simple experiments – on the large-scale interface structure.

Five different spectral shapes were considered for the continuous class, and four of these were also used for the short wavelength component of the bi-component class. In a typical case, random phases were assigned to each mode and randomized amplitudes were selected from the given spectrum. For example, a flat spectrum included modes 4 to 80 with random phases and amplitudes chosen from a uniform distribution. After the amplitude assignment, the resulting spectrum is normalized to give the desired rms amplitude – typically either about $2.5 \mu\text{m}$ (large amplitude case) or $0.25 \mu\text{m}$ (small amplitude case). The other four spectral types include a short wavelength component either with or without a single large amplitude long wavelength mode (mode 4) in order to investigate the effect of short wavelength noise on a long wavelength primary mode. The short wavelength component, which includes modes 20 to 80, is given by either a narrow gaussian centered at mode 40 with half-width ≈ 4 , a broad gaussian centered at mode 40 with half-width 20, a hyperbolic ($1/k$) spectrum, or a $1/k^2$ spectrum. Examples of initial spectra and interface profiles are shown in Fig. 4. Multiple randomized amplitude and phase realizations were generated from each spectral type in order to provide information about the typical level of fluctuations of measurable quantities within each spectrum.

We can characterize continuous spectra by their initial rms amplitude a_{rms} (or $\langle a \rangle_0$), their characteristic wavenumber $\langle k \rangle$ (or characteristic mode number $\langle m \rangle$), the initial degree of linearity $\langle ka \rangle_0$, the initial spectral shape, and the width of the initial spectrum $\Delta k / \langle k \rangle$. For bi-component spectra, we can add to our parameter list the relative rms amplitudes $\langle a \rangle_{0s} / \langle a \rangle_{0l}$, the relative widths of the spectral components $\Delta k_s / \Delta k_l$, and the separation of the relative two components $\langle k_s \rangle / \langle k_l \rangle$ or $(\langle k_s \rangle - \langle k_l \rangle) / (\langle k_s \rangle + \langle k_l \rangle)$. In

the bi-component case, we focus in particular on the relative rms amplitudes and spectral shape. The ratio of characteristic wavelengths is only varied from 9.25 ($1/k^2$ spectrum) to 11.30 (broad gaussian), with the two components always well-separated in k -space (by an order of magnitude). Since the width of the long-wavelength component is in every case a single mode, all variation of the relative spectral widths is left to the short-wavelength component. The initial spectral width can be thought of as one aspect of the spectral shape, and was only considered in this context in the bi-component case.

A list of these parameters is given in Table 1 together with a brief summary of their effect on the large-scale observables in the simulations. Not surprisingly, we found a link between the two measures used to characterize the internal structure. The simulations all exhibit a transition to a well-mixed state (a “2D mixing transition”) that is correlated with a loss of transverse spectral information. Consequently, the effect of the initial conditions on the nonlinear interface structure is represented simply as their effect on the time to transition. Furthermore, transition results in changes in the spike and bubble growth rates, so anything that affects the transition time also affects the perturbation amplitudes and velocities. In the next sections, the information in Table 1 is developed in detail.

IV. Results and discussion

A. Growth of the mix layer

Mix width history plots from 52 2D simulations are shown in Fig. 5. Most of the various trajectories fall in to one or the other of two families. The upper family contains

the runs with the large amplitude ($2.5\ \mu\text{m}$) mode 4 in the initial spectrum with or without a short wavelength small amplitude component. Short wavelength components included in the plot are the narrow gaussian, broad gaussian, or hyperbolic spectrum, or by a single mode 40. The rms amplitude in each case differs from the mode 4 amplitude by less than 1%. The lower family consists primarily of runs with the small amplitude short wavelength component, with mean rms amplitude of about $0.25\ \mu\text{m}$. The standard deviation from the mean rms amplitude is less than 5%, and the maximum deviation is less than 50%. The small amplitude flat spectrum cases are also contained within the lower family. The large amplitude flat spectrum cases initially lie slightly above the upper family, but then fall below it at about 2-3 ns, eventually joining the lower family between 10 and 20 ns. The two curves below the lower family are from runs with rms amplitude of $0.025\ \mu\text{m}$ (upper curve) and $0.0025\ \mu\text{m}$ (lower curve).

Within the lower family, the amplitude is not well correlated with initial rms amplitude variations at the few-percent level. Furthermore, the difference between runs with different spectral shape (but similar initial rms amplitude) is generally not much greater than the difference seen between different amplitude and phase realizations of the same spectrum. This is illustrated in Fig. 6, which compares the bubble amplitude and velocity evolution for several spectral shapes, including two random phase realizations of the same narrow gaussian distribution without amplitude randomization (dotted lines). Solid lines show the amplitude from simulations with a $1/k$ spectrum (upper solid), flat (middle solid), and broad gaussian (lower solid). All five simulations begin with an rms-amplitude of $0.258\ \mu\text{m}$. After 10 ns, the amplitude and velocity difference between the

two narrow gaussian cases is greater than 25% and is at least as significant as the differences arising from the various spectral shapes.

B. Phases of instability growth

In general, the instability evolution can be divided into three phases, as shown in Figure 7. During the early-time phase (Phase I - which actually included the linear early nonlinear, and into the nonlinear regimes), the growth rate is determined by the most unstable mode. RM dominates initially, but only for about 1 ns. During this period, the inverse cascade to larger scales is initiated, and there are up to three generations of bubble merger. The growth rate depends on the rms amplitude, but does not depend strongly on the spectral details. During Phase II, there are changes in the growth rates (sometimes rather abrupt) that result in a strong dependence on the spectral details as well as the initial rms amplitude. Consideration of separate spike and bubble amplitude histories shows that the spike growth is more sensitive than the bubble growth to the initial spectrum. These changes appear to be random and are not well correlated with small changes in the initial rms amplitude or with the spectral shape.

Phase III begins when mode 1 emerges as the dominant transverse scale after up to five bubble merger generations. After this scale is reached, the inverse cascade is halted and the growth is no longer self-similar-like. One would tend to conclude at this point that this signals the end of the calculation's range of validity because the computational box has been "filled" so that end effects corrupt further evolution. In fact, calculations run with twice or even four times the nominal box size generally show no significant change in the perturbation growth history and or the late-time dominant

transverse scale (see Fig. 8). We attribute this to the decaying nature of the driving acceleration. As the acceleration approaches zero, the time to generate larger scales (which even with constant acceleration take longer to form than shorter scales) tends to infinity. Thus the decaying acceleration profile coupled with the finite experiment duration introduces an “effective box size” even in the absence of an experimentally or computationally-imposed physical box size.

C. Quasi-self-similar regime

The main point in plotting all the amplitude trajectories together on one plot (Fig. 5) is to show that they generally diverge in time rather than converge as one might expect during approach to a stationary self-similar bubble distribution. That is, there is no apparent approach to a self-similar regime independent of the initial conditions. This is true even if one considers only those runs from the lower family with only the short wavelength component and with initial rms amplitude of about $0.25 \mu\text{m}$. If one assumes self-similarity (ie that the characteristic transverse scale is a constant fraction of the mix-width) and takes into account the time-dependence of the acceleration and the large-scale velocity gradient present in the zero-order hydro, then the spike and bubble growth in each run can be characterized by a constant factor α (the α of $h(t) = \alpha A g t^2$ models). In a true self-similar regime, the value of this parameter should be a universal constant with weak (if any) dependence on Atwood number.³³ Within the $a_{\text{rms}} = 0.25 \mu\text{m}$, shorts only subgroup, we instead find that α_{bubble} varies over a range of about 0.035-0.065 while α_{spike} varies over 0.050-0.100. This nearly covers the entire range of values reported from different experiments and simulations (see, for example, Ref. 34 and references therein),

though it falls somewhat short of the values reported for spike growth at this Atwood number (as high as 0.120). Thus the assumption of self-similarity does not lead to a useful means of characterizing the instability growth. Instead, memory of the initial conditions is retained throughout the experiment at least in the mix width. Rather than approaching a constant, the similarity parameter (the ratio of characteristic transverse scale to perturbation amplitude) decays in time. The time dependence of the similarity parameter is shown in Fig. 9 for various initial conditions, including examples of each spectral type included in the study, with rms-amplitudes varying over three orders of magnitude. A narrow gaussian with four times the nominal box width and three flat spectrum calculations with twice the nominal box width are included to show that variations in system size (boundary effects) do not change the general behavior of the similarity parameter.

Because of decompression and drive decay, the asymptotic bubble and spike velocities depend on the amplitude and time as well as on the transverse scale and the degree of mix in the layer. The amplitude dependence arises because of the velocity gradient, which is approximately proportional to $\Delta r/t$ and characteristic of a rarefaction fan. Here Δr is the distance in the parallel direction between any two points, in particular the distance from the unperturbed interface to the position of the spike or bubble tip. Thus the contribution of material decompression and stretching to the spike or bubble velocity at a given time is proportional to its amplitude.

We have extended an existing statistical-mechanics bubble merger model³⁵ to include decompression and the time-dependence of the drive.³⁶ Details of the model are

presented in Ref. 36. We note here only that the model prediction (the red line in Fig. 9) also shows a decaying similarity parameter and agrees well with the simulations.

However, there is apparently loss of transverse spectral information and a period of “quasi-self-similar” growth. This is illustrated in two ways Fig. 10. Figure 10(a) shows a time series of log density plots from a small initial amplitude simulation with a flat spectrum (modes 4-80). During this period, which covers the first 10 ns of growth, the inverse cascade to progressively larger scales is apparent. In Fig. 10(b), the images are rescaled so that the mix-width appears approximately constant in time. The similarity in interface structure in the rescaled images shows that the ratio of dominant transverse scale to mix width does not change much over this time interval. Since the value of this ratio does tend to slowly decrease over time as the material decompresses, we refer to this as a “quasi-self-similar” regime.

Figure 10(c) shows log density plots from simulations with different initial spectral types at early and intermediate times (2.4 and 11.5 ns). Early on, the interface structure is clearly correlated with the initial conditions. In particular, mode 40 is apparent in the early-time narrow gaussian image. The later-time images, on the other hand, appear far more similar to one other. As was noted previously, there is a wide spread in the late time amplitude growth, but the dependence on spectral type within that spread is generally not much larger than the variation between different realizations with the same spectral shape.

The loss of transverse spectral information is illustrated more quantitatively in Fig. 11, which compares average 1D density fluctuation spectra at $t = 0$ and $t = 10$ ns for a variety of short-wavelength spectral shapes. The density fluctuation is defined by $\delta\rho(z)$

$= \rho(z) - \langle \rho(z) \rangle$, where $\langle \rho(z) \rangle$ is the z -dependent transverse density average. Each spectrum shown in Fig. 11 is the average of several (typically nine) 1D spectra evenly spaced throughout the interior of the mix region. Despite significant differences in the initial spectral shapes and rms-amplitudes, all transverse spectral information above about mode 10 has been lost by 10 ns, and memory of the initial conditions is retained only in the amplitudes of the long wavelength modes. For runs with the same initial rms-amplitude, the low-mode end of the spectrum is also very similar, suggesting that only memory of the initial amplitude and not the spectral shape has been retained. An inertial range with Kolmogorov $k^{-5/3}$ scaling is visible between modes thirty and eighty. Transverse and parallel turbulent kinetic energy spectra and velocity fluctuation spectra from the same simulations are shown in Figs. 12 and 13, respectively. The fluctuating components of the energy and velocity are defined in the same way as the density fluctuation: $\delta KE_{x,z}(z) = KE_{x,z}(z) - \langle KE_{x,z}(z) \rangle$ and $|\delta v_{x,z}(z)| = |v_{x,z}(z) - \langle v_{x,z}(z) \rangle|$, where “ $\langle \rangle$ ” again denotes transverse average and $KE_{x,z} = \rho v_{x,z}^2$. In each case, the upper solid curve is the parallel (z) component and the lower solid line is the transverse (x) component. By 10 ns, the spectral shape depends weakly on the initial conditions, and both transverse and parallel components exhibit a limited $k^{-5/3}$ inertial range. In most cases, the high-mode end of the spectrum is reasonably well approximated by a k^{-3} scaling.

Scaling laws for the energy spectrum of stationary 2D “turbulence” were first put forward by Kraichnan, who considered an unbounded system into which energy is uniformly injected at some wavenumber k_{inj} .³⁷ At scales larger than the injection scale, he predicted that an inverse energy cascade driven by vortex merger would result in a

Kolmogorov $k^{-5/3}$ scaling. Below the injection scale, a forward enstrophy cascade would give $E(k) \sim k^{-3}$. Recent experiments using flowing soap films agree with Kraichnan's predictions at both high and low wavenumbers.³⁸

Thus our observation of an inertial range with $\approx -5/3$ scaling at lower mode numbers and ≈ -3 scaling at higher mode numbers indicates a transition to 2D turbulence. After establishment of the quasi-self-similar regime, there is little change in the spectra shape except for a steeper slope at the lowest modes [see Fig. 11(f)].

The RT instability can in principle inject energy into the system at all scales in the density spectrum, but the growth of under-resolved modes is inhibited. The upper end of the inertial range in the energy spectra in Fig. 12 corresponds to injection scales at modes resolved by as little as 3 ppw.

The degree of “mixedness”, which Youngs calls the molecular mix fraction,³³ provides a good measure of when the transition to the quasi-self-similar regime takes place. The mixing parameter is defined by

$$\Theta \equiv \frac{\int \langle f(1-f) \rangle dz}{\int \langle f \rangle dz \int \langle 1-f \rangle dz}, \quad (1)$$

where f is the volume fraction of either of the two fluids, the averaging is done in the transverse direction, and the integral is performed in the parallel direction through the extent of the mix region. The mixing parameter time histories from all 52 2D simulations included in Fig. 5 are shown in Figure 14. Again, most of the curves fall into one of two families. The upper family contains runs without the large amplitude mode 4, while the lower family consists of all the runs with the large mode 4. In both cases, there is a clear transition from a state that is not well mixed to a state with higher degree of mixedness

that tends to an asymptotic value between about 0.6 and 0.8. With no large mode 4, this transition occurs within a few ns, and corresponds to the transition to the quasi-self-similar regime. The same transition occurs when the large mode 4 is included in the initial spectrum, but the time to transition is several times longer. Thus the presence of the long wavelength mode delays the transition to a turbulent-like state. Comparison of Fig. 14 with amplitude history plots shows that, in addition to the increase in mixedness, transition to the quasi-self-similar regime is marked by a decrease in the spike velocity and often an increase in the bubble velocity. The spike velocity decreases in particular for the runs with large-amplitude mode 4, where the transition is associated with the breakup of the primary spikes. This breakup allows the spikes' parallel energy to be diverted into the transverse direction and results in a decrease in the effective Atwood number in the mix region. When the initial spectrum gives an array of nearly identical bubbles, transition can allow for bubble competition and the generation of larger scales, resulting in an increase in the velocity of the bubble front.

The effective Atwood number reduction experienced by the spikes due to increased mixing after their breakup results in an increase in the bubble to spike amplitude ratio, shown in Fig. 15 for several representative cases. In the single-mode (mode 4) case, the amplitude ratio approaches a value of about 0.48. This is just slightly higher than the value of $\sqrt{\rho_b / \rho_s} \approx 0.42$ predicted by a buoyancy-drag model assuming that the spike reaches terminal velocity early on.^{5,39} With the spike interaction and breakdown associated with transition to the quasi-self-similar regime, the amplitude ratio is much closer to unity and typically greater than 0.7 at late times. The same tendency towards spike-bubble amplitude symmetry due to spike breakup was reported by Youngs,

who also noted an associated weak dependence of h_b/h_s on the density ratio.³³

In a true self-similar regime (at least for the case of incompressible flow, no RM component, and constant acceleration – all of which are violated here), the post-transition mixedness should be a universal constant depending only on the Atwood number.³³ For a density ratio similar to ours (and with very weak density ratio dependence), Youngs found in his 3D calculations that the asymptotic degree of mix increases at higher resolution where the inertial range is better resolved. Extrapolating the observed trend to infinite resolution, he reports a value of about 0.83 in 3D and 0.54 in 2D.⁴⁰ Cook *et al.* find similar values in their high resolution, classical RT calculations.⁴¹ The values we find are distributed throughout this range, and are consistently higher than the reported 2D value.

Finally, we note that there is no true turbulent mixing transition⁴² in the simulations. This is to be expected due to the low effective Reynolds number and the 2D nature of the simulations. Three dimensional turbulence is characterized by a forward cascade of energy to smaller scales where it is eventually dissipated. Vortex stretching, which is the mechanism of coupling to smaller scales, is fundamentally a 3D process and therefore absent in 2D systems. However, the abrupt increase in mixedness observed in the 2D calculations and associated with the onset of strong spike interaction and breakup is reminiscent of a turbulent mixing transition. While spikes grow without interacting with one another, their energy is directed almost entirely in the parallel direction. When they interact and breakup, a significant fraction of their energy is diverted into the parallel direction (see Fig. 16) and smaller scales are generated via the Kelvin Helmholtz (KH) instability.⁴³ Because of this forward cascade, a 2D system undergoing spike

breakup in a sense temporarily mimics 3D turbulence, and there is an associated “2D turbulent mixing transition”.

D. Resolution study

A resolution study was performed in order to verify adequate convergence of the growth rates and interface structure at the nominal resolution of 512 points across the computational domain (512 ppb). The resolution was varied from 128 to 2048 cells per box width (ppb), or from four times less than to four times greater than the nominal resolution. Log density plots [Fig. 17(a)] and perturbation amplitude histories [Fig. 17(b)] from a series of calculations initialized with the same narrow gaussian (shorts only) spectrum suggest that the mix width and interface structure are reasonable well-resolved at 256 ppb. Even at 128 ppb, the mix width is only reduced by 15-25% relative to the highest resolution case. This is impressive considering that, at 128 ppb, the initially dominant mode (mode 40) is resolved to only 3.2 points per wavelength (ppw). Considering the extreme drive strength and only marginally linear initial conditions, the perturbation becomes nonlinear very quickly and the observed fast convergence is perhaps due to the fast generation of larger, better resolved scales due to mode coupling³⁰ and nonlinear interactions among spikes.⁴³

A plot of the mixing parameter [Fig. 17(c)] as a function of time shows that, in contrast to Youngs’s 3D calculations,³³ there is more mixing at lower resolution where the numerical diffusion is greater. The algorithm used to identify the spike and bubble positions is based on the product of the volume fractions of the two fluids averaged over

the transverse direction (the mix width is by definition bounded by the 2.5% points).

When the outlying spikes are more diffuse due to decreased resolution, the algorithm identifies an edge that corresponds to a smaller spike amplitude. This is the primary reason for the correlation between lower resolution and reduced amplitude.

Density, directed kinetic energy, and velocity spectra from a calculation at the highest resolution (2048 ppb) are shown in Fig. 18. Results from a simulation at the nominal 512 ppb resolution with the same narrow gaussian spectral shape are included for comparison. For each quantity, the low-k end of the inertial range is about the same at either resolution. The high-k end extends to much higher mode numbers in the 2048 ppb case, consistent with its higher numerical Reynolds number and resulting in an inertial range that spans about one decade. The minimum energy injection scale is at about mode 700, which again says that the driving instability injects energy into modes resolved by at least 3 ppw.

E. Dependence of transition time on initial conditions

We have already seen how several of the factors listed in Table 1 affect the large-scale instability evolution. In all stages of the instability, larger initial amplitudes give larger amplitude later on. The initial shape of the short-wavelength spectral component has little effect on the late-time growth, including the time to transition to a turbulent-like state. This statement assumes, however, that the initial spectrum includes multiple modes that are not both commensurate and in phase with one another. Without numerical or physical sources of random noise, such spectra can only lead to a limited inverse cascade that gives rise to stable periodic arrays of bubbles.

We have also seen that there is a correlation between transition to the quasi-self-similar regime, which is characterized by a loss of transverse spectral information, and a “2D mixing transition” to a state characterized by a mixedness of 0.6 - 0.8. What remains is to determine how the various parameters in Table 1 affect the time to transition.

There are several ways in which we can consider how the transition time to the quasi-self-similar “turbulent” state depends on the initial conditions. In this section, we will consider variations of the rms-amplitude (resulting in variation of $\langle ka \rangle$ in addition to $\langle a \rangle$), the effect of varying the short wavelength cutoff for a flat spectrum (variation of $\langle k \rangle$, $\langle ka \rangle$, and $\Delta k / \langle k \rangle$), the effect short wavelength “noise” on a long wavelength primary mode (variation of spectral shape and $\langle k \rangle_s / \langle k \rangle_l$), and the effect of a long wavelength mode on a short wavelength spectral component (variation of $\langle a \rangle_s / \langle a \rangle_l$).

1. Initial rms amplitude and nonlinearity thresholds

In order to quantify the dependence of the transition time on the initial rms-amplitude, three simulations were run in which the peak of the narrow gaussian spectrum (called a_{40}) was varied over three orders of magnitude. The peaks of the initial spectra considered were at $a_{40} = 0.001 \mu\text{m}$, $a_{40} = 0.01 \mu\text{m}$, and at the nominal value of $a_{40} = 0.1 \mu\text{m}$. This corresponds to an initial degree of linearity, expressed as a_{40}/λ_{40} , of $2e-4$, $2e-3$, and $2e-2$, respectively. In each case, the rms-amplitude was about 2.5 times greater than then a_{40} .

Results from the calculations are shown in Fig. 19. Regardless of the initial amplitude, spike interaction begins when $h/\lambda_0 \approx 2$. This nonlinearity threshold for spike interaction is slightly greater with smaller initial nonlinearity h_0/λ_0 . This could be due to

the increased shock-deposited vorticity (RM) or increased instability Mach number in the larger-amplitude cases, or a combination of the two. At the same time spike interaction begins, the spike growth rate begins to saturate and the acceleration of the bubble front begins to decrease. Spike breakup continues until $h/\lambda_0 \approx 5-6$ (again somewhat greater for perturbations initially more linear), at which point the mixing parameter reaches its maximum value and the transverse density fluctuation spectrum has reached its asymptotic form. This signifies the loss of initial transverse spectral information and the emergence of the quasi-self-similar regime. At the same time, the post-transition amplitudes and velocity is strongly dependent on the initial rms amplitude [see Figs. 19(d)-19(e)]. Spike and bubble velocities subsequently increase again as the inverse cascade to larger scales progresses. The same sequence is followed for broader initial spectra, without significant change in the nonlinearity thresholds for spike interaction and transition.

2. Effect of short wavelength modes on large-scale interface structure

We are interested in the effect of short wavelength modes on the global instability development for three primary reasons. First of all, some RT-unstable interfaces in real systems [possibly including the Si/(C+O) interface in core-collapse supernovae]⁴⁴ are characterized by distinct long and short-wavelength spectral components. In order to accurately describe the instability development in such systems, we must first understand the importance of the short-wavelength modes.

Secondly, simulations typically use initial spectra that do not extend all the way down to the viscous cutoffs. If unresolved scales have a significant impact on the large-scale interface structure, then such simulations are inadequate.

Finally, laser-driven instability experiments designed to study supernova hydrodynamics are often limited in modal content, typically to no more than a few prescribed modes plus small-scale noise. Since supernovae are presumably not so limited, the experiments are not truly representative of their astrophysical counterparts if short wavelength modes are important. In both cases, one system (a simulation or a laboratory experiment) is employed to study a second physical system that may be less limited in modal content, and it is important to understand the effect of the unresolved scales.

In this section, we consider the effect of short wavelength modes on the global instability development in two ways. First, we vary the short wavelength cutoff in a series of five simulations with initially flat spectra and observe the resulting variation in growth rates and interface structure. The long wavelength cutoff is in each case mode 4, while the short wavelength cutoffs included in the study are $m_{\max} = \{80, 40, 20, 10, 4\}$ ($m_{\max} = m_{\min} = 4$ for the single mode calculation). This gives initial characteristic mode numbers of $\langle m \rangle = \{42, 22, 12, 7, 4\}$, and relative spectral widths of $\Delta m / \langle m \rangle \approx \{1.8, 1.6, 1.3, 0.9, 0.0\}$. The initial rms-amplitude is set to $0.25 \mu\text{m}$ in each case, giving linearity parameters $\langle a/\lambda \rangle \approx \{0.006, 0.005, 0.004, 0.003, 0.005\}$.

Log density plots at several times are shown in Fig. 20(a) from all but the single mode simulation. There is more mixing early on when the initial spectrum extends to higher mode numbers [see Fig. 20(b)], and the inverse cascade to larger scales proceeds more rapidly. Amplitude history plots show that higher short-wavelength cutoff leads to

faster growth during the first few ns but reduced growth at later times [see Figs. 20(c)-20(d)]. The one exception to this pattern is the $m_{\max} = 80$ case, which ends up growing faster asymptotically than the $m_{\max} = 40$ case due to the emergence of a large single dense spike at about 25 ns.

These observations can be partially explained as follows: Spectra extended to higher mode numbers initially give faster growth because of increased shock-deposited vorticity (RM) and because the RT exponential growth rate $\gamma \propto \sqrt{k}$ in the linear regime. The dominance of high modes ends when the low modes become nonlinear and their velocities begin to saturate at their terminal values. If there were no low- l modes in the initial spectrum, or if their initial amplitudes were sufficiently small, then the growth of low- l modes would be dominated by nonlinear interaction between high- l modes (mode coupling).³⁰ In our case, the initial amplitudes of the low- l modes are of order $a/\lambda \sim 0.05/\sqrt{N}$ where the number of modes N varies from 1 to 81. When N is less than or of order 10, the preexisting low- l modes become nonlinear within a few ns and mode coupling does not play a significant role. This is evident in the $m_{\min} = 10$ and $m_{\min} = 20$ log density time series, in which it is apparent that the large wavelength structure at 11.4 ns is correlated with that at 2.4 ns. The difference in the late time growth rates is partially a reflection of the initial amplitudes of the low- l modes that begin to dominate the growth early on. These amplitudes are decreased when we increase the relative spectral width $\Delta k/\langle k \rangle$ while holding the initial rms amplitude constant.

In addition to larger initial amplitudes in the long-wavelength modes, spectra with lower high-mode cutoff give faster growth because they transition to turbulence later. Consequently, they experience less of the density-gradient stabilization associated with

enhanced mixing in the post-transition state. A modified $m_{\max} = 80$ interface was constructed to isolate the effect of enhanced mixing from the initial-amplitude effect. In the modified initial spectrum, the first 7 modes in the $m_{\max} = 80$ spectrum were simply replaced with the spectrum from the $m_{\max} = 10$ case. Because of this change, the initial rms amplitude is just under $\sqrt{2}$ times greater than in the other cases, and the low l -mode amplitudes are the same as in $m_{\max} = 10$ case. Despite the increase in rms amplitude and a large increase in the number of unstable modes, the post-transition growth of the mix region is decreased rather than increased relative to the $m_{\max} = 10$ calculation [see Fig. 20(e)]. In fact, the resulting late-time amplitude history lies below the $m_{\max} = 20$ curve and only rises above the $m_{\max} = 40$ curve at about 12 ns. Thus the presence of the short wavelength modes leads to a significant reduction in the nonlinear growth of the mixing layer.

The opposite effect was found by Milovich *et al.* in simulations of NIF double-shell ignition target designs.⁴⁵ In the double shell targets, instabilities develop on a metal/foam interface during capsule implosion. The perturbation spectrum was taken from measurements of an Omega glass capsule, and a series of calculations was run in which the number of modes was increased from about 40 up to several hundred. The angular resolution was determined such that the shortest-wavelength mode in the initial conditions was resolved to at least 20 ppw, and l_{\min} was set to 12 in each case. The late-time perturbation growth was found to increase with increasing l_{\max} , with a particularly dramatic increase when l_{\max} was increased from 102 to 204. There are several differences between their system and ours that might contribute to this discrepancy. First of all, the number of modes is varied much more widely in their calculations than in our, and their

initial spectrum falls off relatively slowly above mode 50. Since they do not renormalize the initial spectrum each time, runs with more modes have greater initial rms amplitudes. Secondly, modes in their initial spectrum are typically far more linear than ours. This allows more time for short-wavelength modes to couple and generate larger scales during the weakly nonlinear regime before saturation. The most significant difference, however, is that their low- l modes do not have time to grow from the initial conditions up to nonlinear amplitudes. With $l_{\max} = 54$, the perturbations at ignition time (the end point of the calculation) remain linear. Even with $l_{\max} = 102$, the low- l modes appear to have attained a degree of nonlinearity $a/\lambda \sim 1$. When l_{\max} is increased to 204, however, the late-time perturbations are very nonlinear and scales larger than the initial conditions have been generated. This indicates that significant mode coupling and associated pumping of large scales to nonlinear amplitudes is possible only with $l_{\max} > 200$. In our system, the low- l modes do not have to rely on mode coupling in order to reach large amplitudes on the time-scale of the experiment. Since the addition of shorter wavelengths does not increase the initial rms amplitude by more than a factor of $\sqrt{2}$, its main effect is to hasten the transition to a state with lower effective Atwood number and greater energy isotropy.

An extensive series of calculations was run to investigate the effect of short wavelength modes on the evolution of a single long wavelength mode. The long wavelength mode is mode 4, with nominal initial amplitude of $2.5 \mu\text{m}$. The short-wavelength component is bounded by modes 20 and 80, and typically has an rms-amplitude that is $1/10$ that of the nominal mode 4 amplitude. The shape of the short-wavelength spectral component was either narrow gaussian, broad gaussian, hyperbolic ($1/k$), or $1/k^2$ [see Fig. 4(a)]. A representative initial interface profile (with a $1/k$ short

wavelength component) is shown in Fig. 4(e). Changes in spectral shape result in small changes in the characteristic mode number of the short wavelength component, and hence in the k-space separation parameter $\langle k \rangle_s / \langle k \rangle_l$, which varies over 9.25-11.30. These simulations make up the upper family of amplitude history curves in Figs. 5(a) and 7(a) and the lower family of mixing parameter curves in Fig. 14. The single-mode amplitude history (no short-wavelength component) is the uppermost curve in the large-amplitude family, indicating that the short-wavelength component reduces the late-time perturbation growth by as much as 20%. Plots of separate spike and bubble amplitude histories (not included) show that there is twice as much variation (about 30%) in the spike amplitudes as there is in the bubble amplitudes (about 15%).

We found in section IV.A that the location of a given curve within the small-amplitude family of Figs. 5 and 7 is not well correlated with the spectral shape. The same is true for the bi-component upper family. Figure 21 includes amplitude history plots from the single mode calculation, mode 4 plus hyperbolic shorts (with $\langle k \rangle_s / \langle k \rangle_l = 10.75$), and mode 4 plus broad gaussian shorts (with $\langle k \rangle_s / \langle k \rangle_l = 11.30$). The difference in amplitude between the two mode-4-plus-shorts cases is characteristic of the differences seen between different short-wavelength spectral shapes or different randomized amplitude and phase realizations of the same spectral shape. Again, the shape of the initial spectrum is not important in determining the late-time large-scale interface structure.

The principle effects of short wavelength modes on the large-scale interface structure are to increase the degree of mixing and accelerate the transition to the quasi-self-similar “turbulent” state [see Fig. 21(a)]. Both of these effects involve the interaction

and breakup of spikes and an associated significant reduction in the overall growth rate of the spike front [see Fig. 21(b)]. The single mode spikes eventually break down as well under the influence of a numerical noise that effectively adds a short wavelength component. This happens later in time though, indicating that the rms amplitude of the short-wavelength is important in determining its effect on the long-wavelength mode. The late-time growth rate of the bubble front is increased if the breakup of spikes allows for bubble competition and merger on what would otherwise be a stable periodic array of bubbles [see Fig. 21(c)]. Because of the strong influence of the short-wavelength component on the transition time, coupled with the strong effect of transition on the global characteristics of the flow, systems comprised of a single mode or a few commensurate modes make poor surrogates for real physical systems. For broadband spectra, it appears that the presence and rms amplitude of the short wavelength component but not its spectral shape are important. This suggests that computational or experimental surrogates for systems dominated early on by long-wavelength modes need not accurately reproduce the details of the short-wavelength spectral component as long as the low l -modes are well resolved. Because this scenario might depend on the dimension of the perturbation, we will consider in a later paper the effect of unresolved modes on the evolution of 3D systems capable of undergoing a turbulent mixing transition.

3. Variation of $\langle a \rangle_s / \langle a \rangle_l$

Finally, we consider the variations in the relative rms amplitudes of the long and short-wavelength components. We ran a series of five calculations, each of which

included the same narrow gaussian short-wavelength spectrum plus mode 4. The relative amplitude parameter $\langle a \rangle_s / \langle a \rangle_l$ was controlled by varying the mode 4 amplitude from 0.0 to 2.5 μm , with intermediate values of 0.025, 0.25, and 1.0 μm . The results are depicted in Fig. 22. When the initial amplitude of mode 4 is less than or equal to the rms amplitude of the short-wavelength component ($\langle a \rangle_s / \langle a \rangle_l \geq 1$), the instability evolution closely resembles the shorts-only case. The transition time in particular is not sensitive to the presence or amplitude of mode 4 as long as its amplitude is small [see Fig. 22(b)]. When the mode-4 amplitude is larger than $\langle a \rangle_s$, there is a qualitative change in the instability development. Mode 4 begins to dominate the growth within a few ns, in a time that is roughly equal to or less than the time required for the short-wavelength modes to reach their nonlinearity thresholds and undergo transition. Shear that develops along the mode-4 spikes and bubble as they grow into the nonlinear regime greatly inhibits the development of small-scale structure and delays the time to transition [see Fig. 22(a)]. This delay contradicts what one would expect based on transition to shear-layer turbulence, which should appear earlier along larger spikes due to their faster terminal velocities and consequently higher Reynolds numbers. The same stabilizing effect was noted and described by Ofer *et al.* in their discussion of the effect of a secondary long-wavelength mode on a short-wavelength primary mode⁴⁶, and is also visible in a calculation by Youngs.⁵ The short-wavelength spectral component is in large part lost and must be regenerated later after the mode-4 spikes reach their interaction and transition nonlinear thresholds.

V. Comparison with classical case

Some of the results we have found in our 2D, high-resolution simulations of blast-wave-driven systems are applicable to classical RT systems, while others are not.

Potential sources of differences are the time-dependence of the drive and compressibility.

Compressibility effects include the RM contribution, moderately high instability Mach number (up to $M^2 \sim 0.1$ in our calculations), stretching of perturbations due to material decompression, and the associated density gradient behind the shock front.

Our “effective box size”, which arises because of the decay of the driving acceleration, is absent in classical systems. However, most if not all multi-merger-generation experiments and simulations performed to date are affected by a physical or computational box size at late times.

The process of spike interaction and breakup will likely proceed similarly in both systems. However, we might expect to find lower nonlinearity thresholds in our case due to shock-deposited vorticity and higher instability Mach number. From classical RT simulations of Ofer *et al.*, it appears that spike interaction begins at about $h/\lambda \sim 2-3$.⁴⁶ This might be slightly higher than our value of $h/\lambda \sim 2$, but the difference seems too small to be meaningful.

In planar blast-wave-driven systems, a true self-similar regime independent of initial conditions is not possible due to decompression. We have found in its place a quasi-self-similar regime that is limited in time and transverse scale due to drive decay. Self-similarity in classical RT systems remains a possibility (but even there has not yet been conclusively demonstrated), and we might expect a correspondence between transition requirements in classical systems and the onset of quasi-self-similar growth in

blast-wave-driven systems. Early rocket-rig experiments⁶ and simulations⁵ suggested self-similar-like growth after about 2.5 generations of bubble merger. This is frequently expressed as the requirement that transverse scales ten times larger than the most unstable mode or the initial characteristic scale must be generated in order to transition to take place. More recent water-channel experiments are also consistent with this requirement.⁴⁷ After 2.5 merger generations, the initial characteristic mode 40 in our shorts-only calculations has shifted to mode 7. According to Fig. 8, this occurs at about 6 ns. The observed transition time, based on the mixing parameter or the loss of transverse spectral information, is at about 3-4 ns or after just one merger generation. Again, this accelerated transition is likely due to enhanced vorticity due to RM and very fast spike growth, both of which might facilitate spike interaction and breakdown. In 2D calculations with instability Mach number of the same order as ours (but without a shock), Glimm *et al.* report spike interaction and transition to a “multiply connected structure” after about 1.5 merger generations.⁴⁸ The fact that they consider this transition (and the resulting growth rate reduction) to be an unphysical 2D artifact points to the need for comparison with highly-resolved 3D calculations.

Despite the decreased drag on 3D objects and the suggestion that the post-transition growth reduction in 2D calculations is artificial, early 3D classical RT calculations by Youngs show reduced growth relative to the 2D case in the turbulent regime.⁴⁹ This reduction is likely due to increased dissipation in 3D, as suggested by Youngs in the same paper. A similar effect has been observed in ongoing state-of-the-art simulations by Cook *et al.*, who consider the instability growth in terms of four evolutionary stages.⁴¹ After a short period of independent modal growth, a mode-mode

interaction phase begins when $h/\langle\lambda\rangle \sim 2$ (equal to our threshold for spike interaction). During this “weak turbulence” phase, the mixing parameter reaches a local maximum at $h/\langle\lambda\rangle = 4.3$ (similar to our peak at $h/\langle\lambda\rangle \sim 5$). A second increase in the mixing parameter occurs between $h/\langle\lambda\rangle \sim 8$ -19, which they call the turbulent mixing transition. The mixing and similarity parameters appear to have reached their asymptotic values by about $h/\langle\lambda\rangle = 19$, which marks the beginning of a strong turbulence phase that extends to the end of their calculation at $h/\langle\lambda\rangle = 30$. In some of our 2D calculations, we too see a second peak in the mixing parameter [see Fig. 19(b) for an example] approached over about $h/\langle\lambda\rangle \sim 14$ -24. We find these parallels encouraging in light of the high-resolution, high-order nature of the Cook *et al.* calculations along with our expectation that transition should proceed qualitatively similarly in classical and blast-wave-driven systems. More detailed comparisons, however, will have to await completion of our 3D blast-wave-driven simulations.

VI. Conclusions

We have presented and discussed results from a series of over 70 2D high-resolution AMR simulations of hydrodynamically-unstable interfaces driven by a strong blast wave under NIF-like drive conditions. The mix-width time histories show no apparent approach to a self-similar regime independent of the initial conditions. This is due to decompression and drive decay, which result in an asymptotic velocity that depends on the amplitude and time as well as on the transverse scale and the degree of

mix in the layer. For sufficiently long but finite experiment duration, drive decay also leads to an effective box size that sets a maximum transverse scale that can be generated. After this scale is reached, the inverse cascade is halted and the growth is no longer self-similar-like. There is, however, a period of quasi-self-similar growth after generation of scales larger than the initial conditions but before the generation of the effective-box-size scale.

The existence of the quasi-self-similar state and the drive-imposed effective box size make the blast-wave-driven case distinct from classical RT. However, transition to the quasi-self-similar state is very similar to its classical counterpart. In both cases, transition is marked by an increase in the degree of mixedness, a decrease in the spike velocity, and often an increase in the bubble velocity.

For continuous and bi-component (short on long) spectra, we have identified several parameters that classify and characterize the initial conditions. We have investigated how variations of a subset of these parameters can affect the observable properties of the deep nonlinear instability evolution. We found, for example, that a long wavelength mode can inhibit the development of small scales and delay the transition to a turbulent-like state when its amplitude is larger than the rms amplitude of the short-wavelength spectral component.

Most notably, apparently random variations observed in late-time amplitudes and growth rates were not well correlated with initial spectral shape. The presence of the short wavelength component is important for facilitating the transition to turbulent-like flow, but its effect on the large scales does not depend strongly on its spectral shape. Only the average properties are important, such as the initial rms amplitude and

characteristic wavenumber. This bodes well for simulations of similarly strongly-driven systems that leave a portion of the short-wavelength end of the spectrum unresolved. As long as the system contains some fast-growing and interacting modes that can be resolved computationally or reproduced experimentally (and has the correct initial rms amplitude), the late-time instability evolution will likely closely resemble the fully resolved or complete system. This reaffirms the hope that laser-driven experiments can serve as useful and relevant platforms for studying compressible mixing in supernova despite their drastically more limited available range of scales. Similarly, carefully-designed numerical simulations need not necessarily reproduce the full range of spectral details present in their physical counterparts in order to reasonably reproduce the late-time large-scale interface structure. These conclusions apply in particular to systems with long-wavelength modes large enough in amplitude to reach the nonlinear phase early on.

It is important to remember that these conclusions are based solely on 2D calculations and might be altered somewhat in 3D. In a later paper, we will extend the discussion and analysis to high-resolution 3D simulations currently underway. This analysis will include a discussion of the effects of initial conditions on the turbulent mixing transition and the nature of the subsequent turbulent flow.

VII. Acknowledgements

This work was performed under the auspices of the U. S. Department of Energy by the University of California, Lawrence Livermore National Laboratory under contract No. W-7405-Eng-48.

VIII. References

- ¹J. W. S. Rayleigh, *Scientific Papers* (University press, Cambridge, 1899).
- ²G. I. Taylor, Proc. R. Soc. London, Ser. A **201**, 192 (1950).
- ³J. Glimm, D. H. Sharp, Phys. Rev. Lett. **64**(18), 2137 (1990).
- ⁴U. Alon, J. Hecht, D. Mulamel, and D. Shvarts, Phys. Rev. Lett. **72**(18), 2867 (1994).
- ⁵D. L. Youngs, Physica D **12**, 32 (1984).
- ⁶K. I. Read, Physica D **12**, 45 (1984).
- ⁷W. D. Arnett, J. N. Bachall, R. P. Kirshner, and S. E. Woosley, Ann. Rev. Astron. Astrophys. **27**, 629 (1989).
- ⁸W. Hillebrandt and P. Hoflich, Rep. Prog. Phys. **52**, 1421 (1989).
- ⁹R. D. Richtmyer, Commun. Pure Appl. Math. **13**, 297 (1960).
- ¹⁰E. E. Meshkov, *Izv. AN SSSR Mekhanika Zhidkosti i Gaza* **4**(5), 151 (1969).
- ¹¹R. Chevalier, Ap. J. **207**, 872 (1976).
- ¹²J. Kane, D. Arnett, B. A. Remington, S. G. Glendinning, G. Bazan, R. P. Drake, B. A. Fryxell, R. Teyssier, and K. Moore, Phys. Plasmas **6**(5), 2065 (1999).

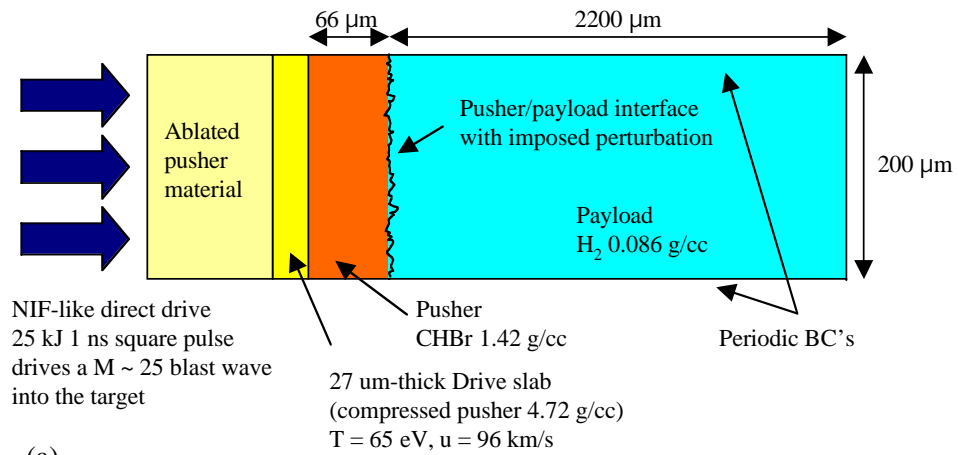
- ¹³A. R. Miles, D.G. Braun, M.J. Edwards, H.F. Robey, R.P. Drake, *et al.*, “Numerical Simulation of Supernova-Relevant Laser-driven Hydro Experiments on OMEGA”, submitted to *Phys. Plasmas*.
- ¹⁴D. Arnett, B. Fryxell, E. Muller, *Astrophys. J.* **341**, L63 (1989); E. Muller, B. Fryxell, D. Arnett, *Astron. Astrophys.* **251**, 505 (1992)
- ¹⁵B. A. Remington, J. Kane, R. P. Drake, *et al.*, *Phys. Plasmas* **4**, 1994 (1997).
- ¹⁶E. M. Campbell, *Las. Part. Beams* **9**, 209 (1991).
- ¹⁷J. M. Soures, R. L. McCrory, C. P. Verdon, *et al.*, *Phys. Plasmas* **5**, 2108 (1996).
- ¹⁸K.S. Budil, B.A. Remington, T.A. Peyser, K.O. Mikaelian, P.L. Miller, *et al.*, *Phys. Rev. Lett.* **76**, 4536 (1996).
- ¹⁹J. Kane, D. Arnett, B.A. Remington, S.G. Glendinning, J. Castor, *et al.*, *Astrophys. J.* **478**, L75 (1997).
- ²⁰J. Kane, D. Arnett, B.A. Remington, S.G. Glendinning, R. Wallace, *et al.*, in *Second Oak Ridge Symposium on Atomic and Nuclear Astrophysics*, Oak Ridge, Tennessee, 1998).
- ²¹J. Kane, D. Arnett, B.A. Remington, S.G. Glendinning, G. Bazan, *et al.*, *Astrophys. J. Suppl.* **127**, 365 (2000).
- ²²J.O. Kane, H.F. Robey, B.A. Remington, R.P. Drake, J. Knauer, *et al.*, *Phys. Rev. E* **63**, 055401R (2001).
- ²³H.F. Robey, J.O. Kane, B.A. Remington, R.P. Drake, O.A. Hurricane, *et al.*, *Phys. Plasmas* **8**, 2446 (2001).
- ²⁴R.P. Drake, H.F. Robey, O.A. Hurricane, Y. Zhang, B.A. Remington, *et al.*, *Astrophys. J.* **564**, 896 (2002).

- ²⁵H.F. Robey, Y. Zhou, A.C. Buckingham, P. Keiter, B.A. Remington, *et al.*, Phys. Plasmas **10**, 614 (2003).
- ²⁶E. M. Campbell, Laser Part. Beams, **9**(2), 209 (1991).
- ²⁷L. H. Howell and J.A. Greenough, J. Comp. Phys. **184**, 53 (2003).
- ²⁸E. M. Corey and D. A. Young, UCRL-JC-127698. Lawrence Livermore National Laboratory, Livermore, CA (1997).
- ²⁹G. B. Zimmerman and W. L. Kruer, Comments on Plasma Physics and Controlled Fusion **2**, 51 (1975).
- ³⁰S. W. Haan, Phys. Fluids B **3**(8), 2349 (1991).
- ³¹S. W. Haan, Phys. Rev. A **39**(11), 5812 (1989).
- ³²D. Ofer, U. Alon, D. Shvarts, R. L. McCroy, and C. P. Verdon, Phys. Plasmas **3**(8), 3073 (1996).
- ³³D. L. Youngs, Phys. Fluids A **3**(5), 1312 (1991).
- ³⁴G. Dimonte, Phys. Plasmas **7**(6), 2255 (2000).
- ³⁵U. Alon, D. Shvarts, and D. Mukamel, Phys. Rev. E, **48**(2), 1008 (1993).
- ³⁶A. R. Miles, “Bubble merger model for the nonlinear Rayleigh-Taylor instability driven by a strong blast wave”, submitted to Phys. Plasmas.
- ³⁷R. H. Kraichnan, Phys. Fluids **10**, 1417 (1967).
- ³⁸M. A. Rutgers, Phys. Rev. Lett. **81**(11), 2244 (1998).
- ³⁹D. Oron, L. Arazi, D. Kartoon, A. Rikanati, U. Alon, and D. Shvarts, Phys. Plasmas **8**(6), 2883 (2001).
- ⁴⁰D. L. Youngs, Las. Part. Beams **12**(4), 725 (1996).

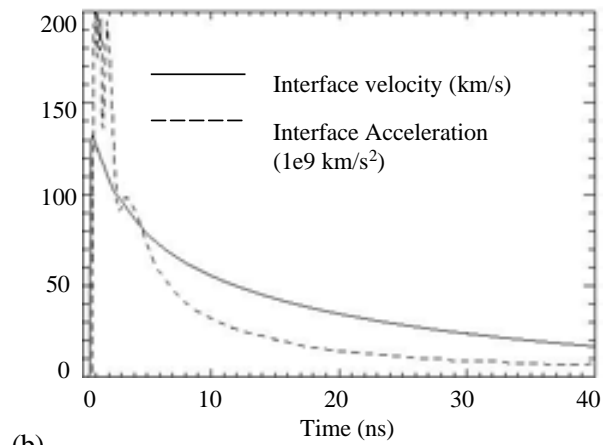
- ⁴¹A. W. Cook, W. H. Cabot, P. L. Miller, P. E. Dimotakis, and T. W. Mattner, “Effects of mixing on Rayleigh-Taylor instability”
- ⁴²P. E. Dimotakis, J. Fluid Mech. **409**, 69 (2000).
- ⁴³A. R. Miles, M.J. Edwards, B. Blue, J. F. Hansen, H.F. Robey, *et al.*, “The effect of a short-wavelength mode on the evolution of a long wavelength perturbation driven by a strong blast wave”, submitted to Phys. Plasmas.
- ⁴⁴K. Kifonidis, T. Plewa, H.-Th. Janka, and E. Muller, Astron. Astrophys. **408**, 621 (2003).
- ⁴⁵J. L. Milovich, P. Amendt, M. Marinak, and H. Robey, Phys. Plasmas **11**(4), (2004).
- ⁴⁶D. Ofer, D. Shvarts, Z. Zinamon, and S. A. Orszag, Phys. Fluids B **4**(11), 3549 (1992).
- ⁴⁷D. M. Snider and M. J. Andrews, Phys. Fluids **6**(10), 3324 (1994).
- ⁴⁸J. Glimm, X. L. Li, R. Menikoff, D. H. Sharp, and Q. Zhang, Phys. Fluids A **2**(11), 2046 (1990).
- ⁴⁹D. L. Youngs, Laser and Part. Beams **12**(4), 725 (1994).

Spectral parameters	Range of parameter variation and Notes	Effect of parameter increase on: Perturbation amplitudes and growth rates	Effect of parameter increase on: Time to transition
Continuous spectra			
rms amplitude $\langle a \rangle$	0.0025 μm - 2.5 μm	Increase	Decrease
Characteristic wavelength $\langle k \rangle$	$\langle m \rangle = 4-46$	Decrease	Decrease
Initial nonlinearity $\langle ka \rangle$	$\langle a/\lambda \rangle = 5e-4 - 5e-2$ Sets thresholds for spike interaction and transition.	Effect contained in individual dependence on $\langle a \rangle$ and $\langle k \rangle$	Decrease
Spectral shape	Single mode, flat, narrow gaussian, broad gaussian, $1/k, 1/k^2$	Little effect	Little effect
Spectral width $\Delta k / \langle k \rangle$	0 - 1.8 Not varied independent of $\langle k \rangle$	Decrease for given k_{\min}	Decrease for given k_{\min}
Bi-component spectra (long + shorts)			
Shorts/longs rms amplitude ratio $\langle a \rangle_s / \langle a \rangle_l$	(< 0.001) - 0.1 Effect on bubble growth may be opposite for multimode long-wavelength component	Decrease for spikes and increase for bubbles	Decrease
Spectral shape of shorts	Narrow gaussian, broad gaussian, $1/k, 1/k^2$	Little effect	Little effect
Spectral shape of longs	Not varied		
Ratio of characteristic wavelengths $\langle k \rangle_s / \langle k \rangle_l$	9.50-11.30 Not varied independent of shape.	Little effect over range considered	Little effect over range considered
Ratio of spectral widths $\Delta k_s / \Delta k_l$	Not varied independent of relative amplitude and shape	Inconclusive	Inconclusive

Table 1: List of the parameters used to classify and characterize the initial spectral conditions and a summary of their effect on the nonlinear instability evolution. See text for detailed explanation.



(a)



(b)

Figure 1: (a) Target schematic (not to scale). (b) Variation in time of interface velocity and deceleration.

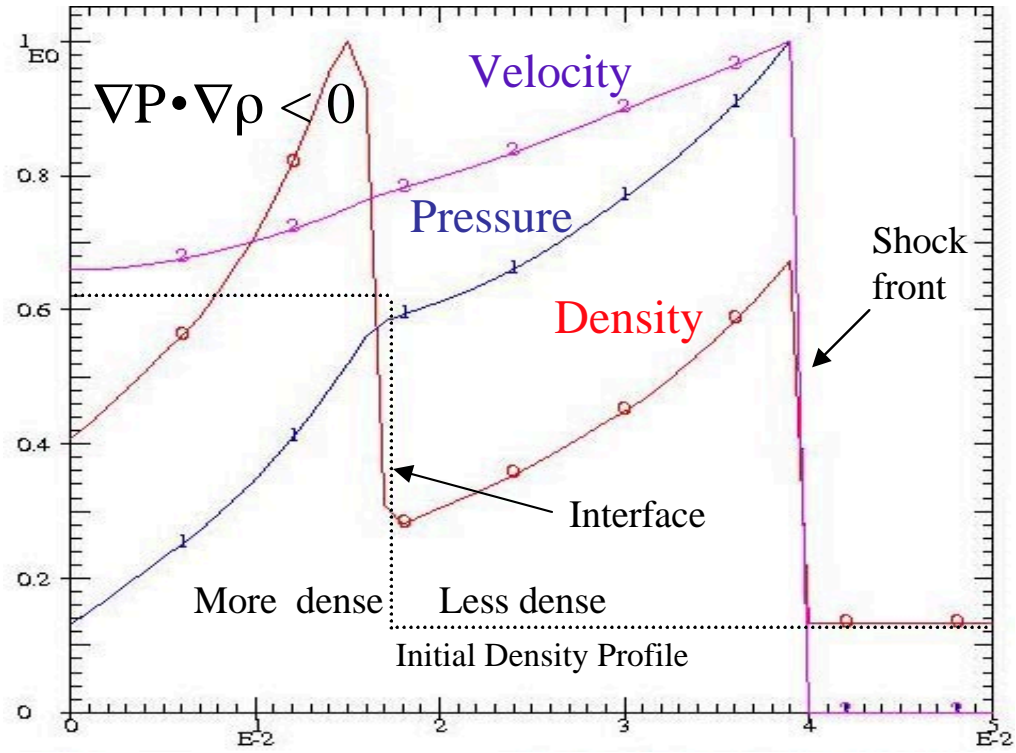


Figure 2: Pressure, density, and velocity profiles (normalized to their maximum values) after refraction of a 1D blast wave through a heavy-light interface in the target. The Rayleigh-Taylor instability criterion is satisfied at the post-shock interface, which is also Richtmyer-Meshkov unstable. The fluid velocity falls off approximately linearly behind the shock front. The corresponding decompression results in additional perturbation growth.

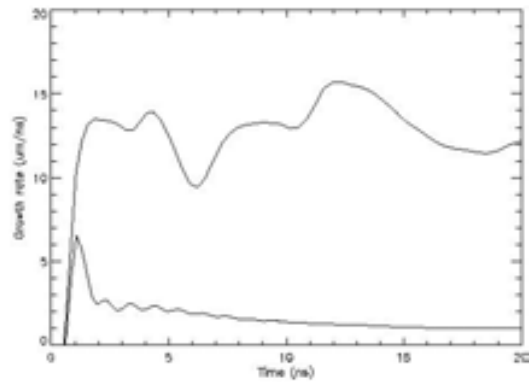


Figure 3: Comparison of pure RM and blast-wave-driven (RT+RM+decompression) growth rates suggest that RT+stretching effects dominate after about 1 ns of instability growth.

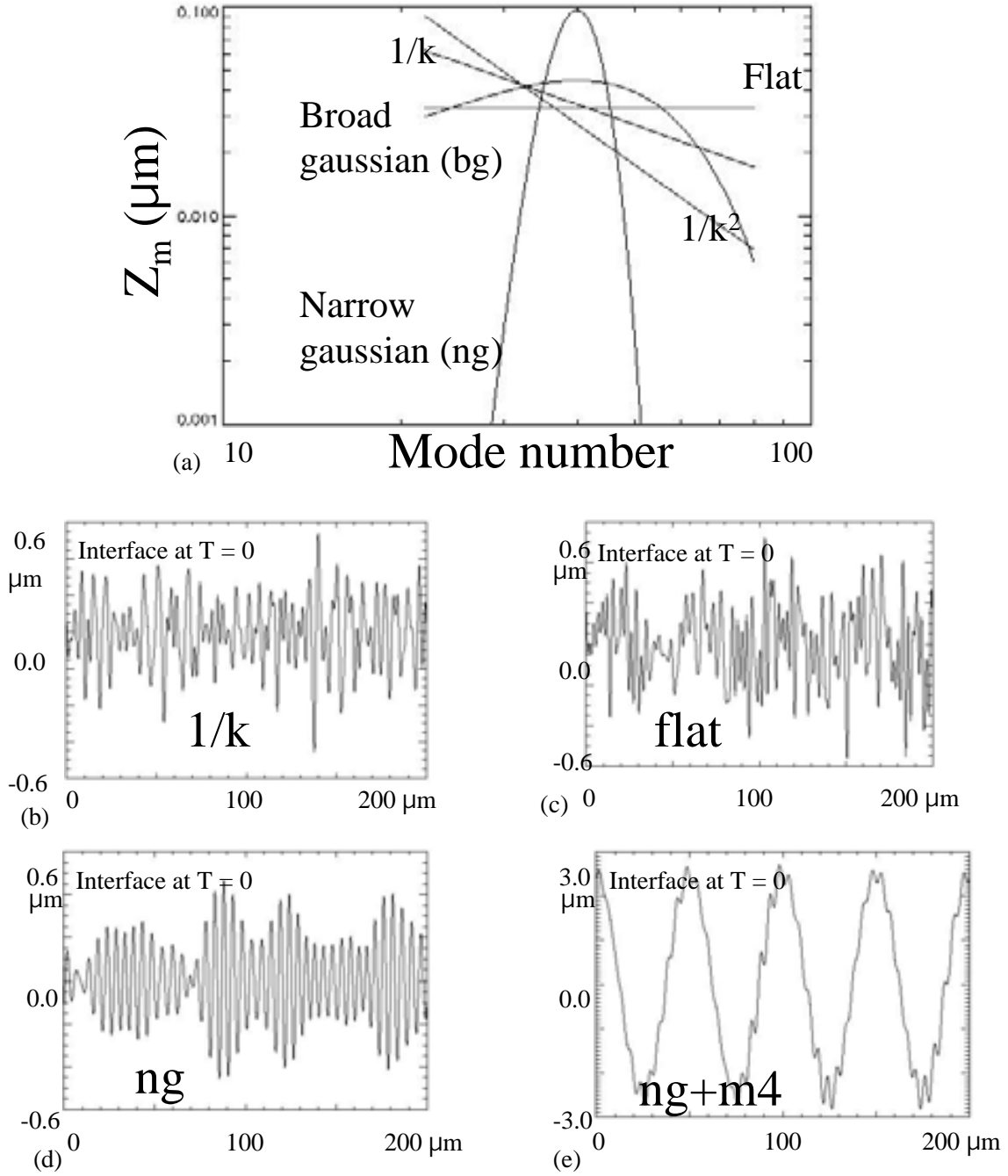


Figure 4: (a) Initial spectral shapes and typical interface profiles: (b) hyperbolic ($1/k$), (c) flat, (d) narrow gaussian, (e) and narrow gaussian with large-amplitude mode 4.

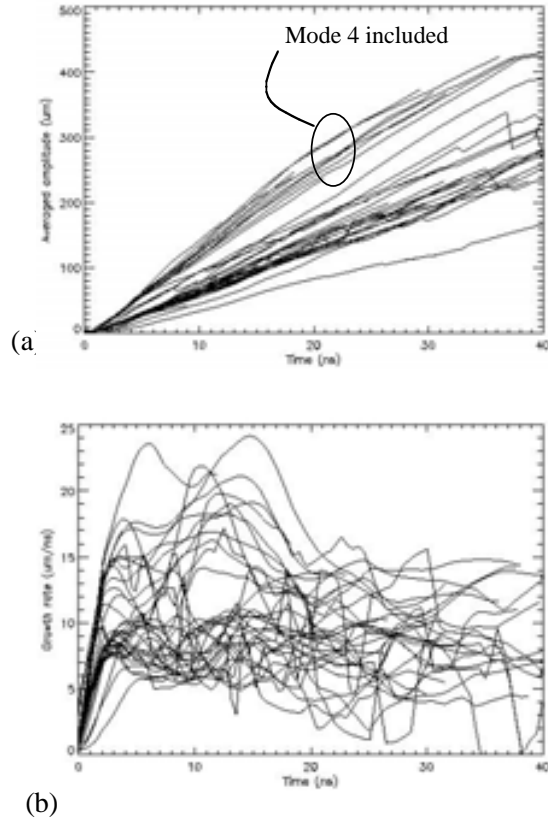


Figure 5: (a) Mix width histories and (b) growth velocities from 52 2D simulations with different spectral initial conditions. There is no apparent approach to a self-similar regime independent of the initial conditions. Even when runs with large mode 4 are excluded, α_b varies over a range of about 0.035-0.065 for different IC's, while α_s varies over about 0.050-0.100.

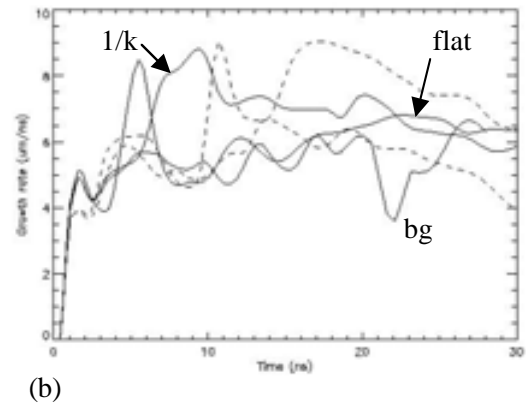
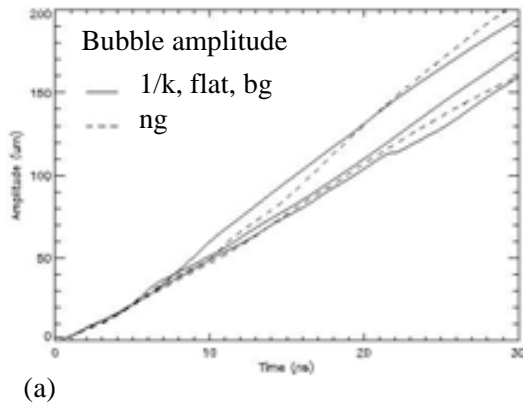


Figure 6: Sensitivity of bubble (a) amplitude and (b) velocity to spectral shape. Solid lines denote three initial spectra: 1/k [upper solid in (a)], flat [middle solid in (b)], and broad gaussian [lower solid in (a)]. The dotted lines denote two phase realizations of the same narrow gaussian spectrum. In each case, the initial rms-amplitude is $0.258 \mu\text{m}$.

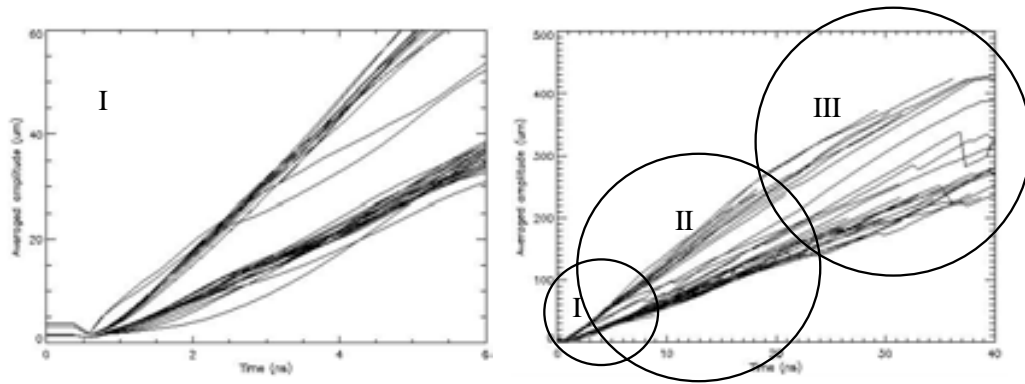


Figure 7: Three phases of instability growth. Phase I: The early-time (linear, early nonlinear, and into nonlinear) phase is dominated by RM for about 1 ns. The growth rate is determined by the most unstable mode, and the inverse cascade is initiated. Phase II: Changes in growth rate result in strong dependence on spectral details in addition to the initial a_{rms} . Phase III: Mode 1 emerges as the dominant transverse scale after up to 5 bubble merger generations. The acceleration profile introduces an “effective box size”. The asymptotic velocity depends on amplitude, time in addition to the transverse scale and the degree of mix in the layer.

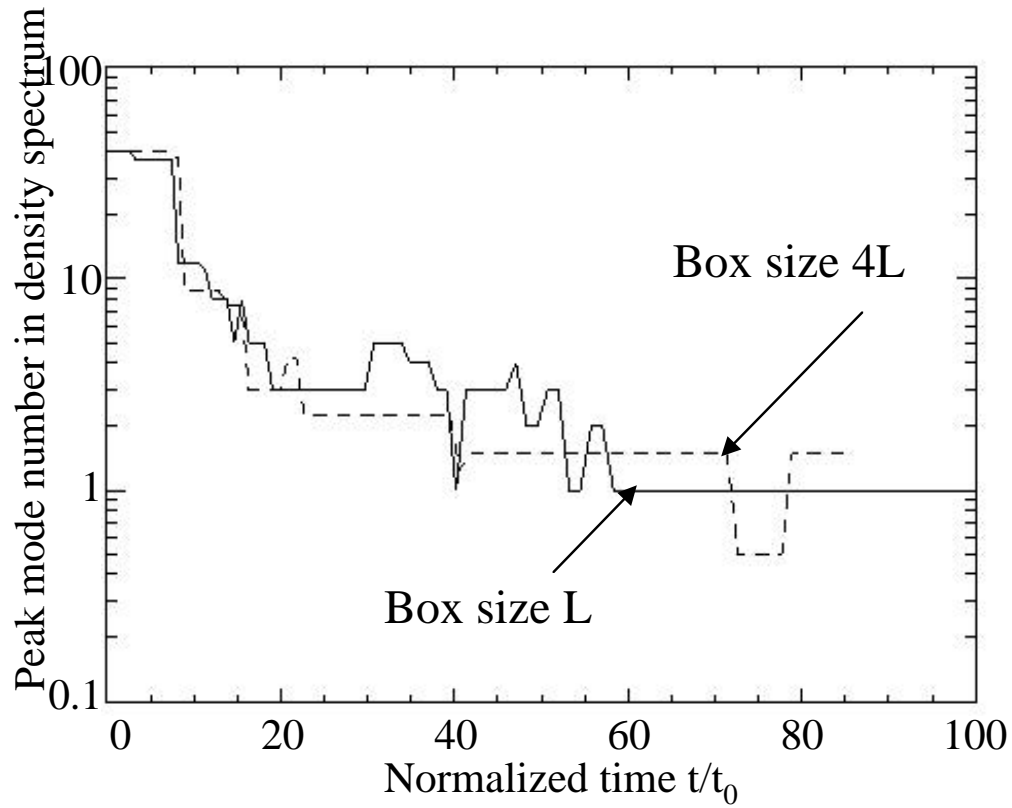


Figure 8: “Effective box size” imposed by the decaying nature of the drive coupled with the finite duration of the experiment. With a box-size of $L = 200 \mu\text{m}$, mode 1 emerges as the dominant mode at about $t/t_0 = 60$ (24 ns). Even when the width of computational domain is quadrupled, longer-wavelength modes do not dominate at late times. After 25 ns, the time required to generate lower l -modes exceeds the time remaining in the experiment. Both cases use the same narrow gaussian spectral shape.

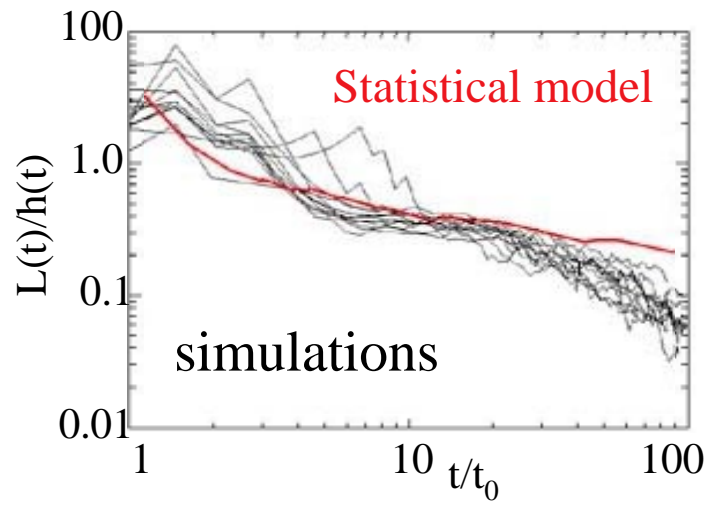


Figure 9: Time-dependence of the similarity parameter. Because of decompression, the similarity parameter decays in time rather than approaching a constant asymptotic value. This behavior is well-predicted by a statistical-mechanics bubble merger model that includes decompression and the time-dependence of the drive.

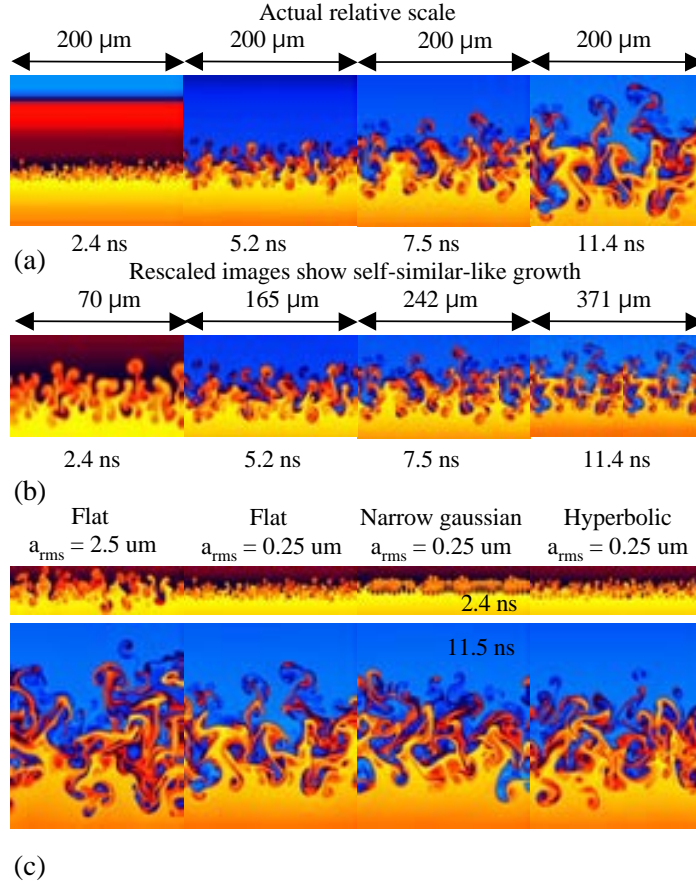


Figure 10: Quasi-self-similar regime. (a) A time series of log density plots from a small initial amplitude simulation with a flat spectrum (modes 4-80) shows the inverse cascade to progressively larger scales. (b) The same images are rescaled so that the mix-width appears approximately constant in time. The similarity in interface structure in the rescaled images shows that the ratio of dominant transverse scale to mix width does not change much over this time interval. (c) The loss of transverse spectral information is illustrated by log density plots from simulations with different initial spectral types at early and intermediate times (2.4 and 11.5 ns). Early on, the interface structure is clearly correlated with the initial conditions. The later-time images appear far more similar to one other.

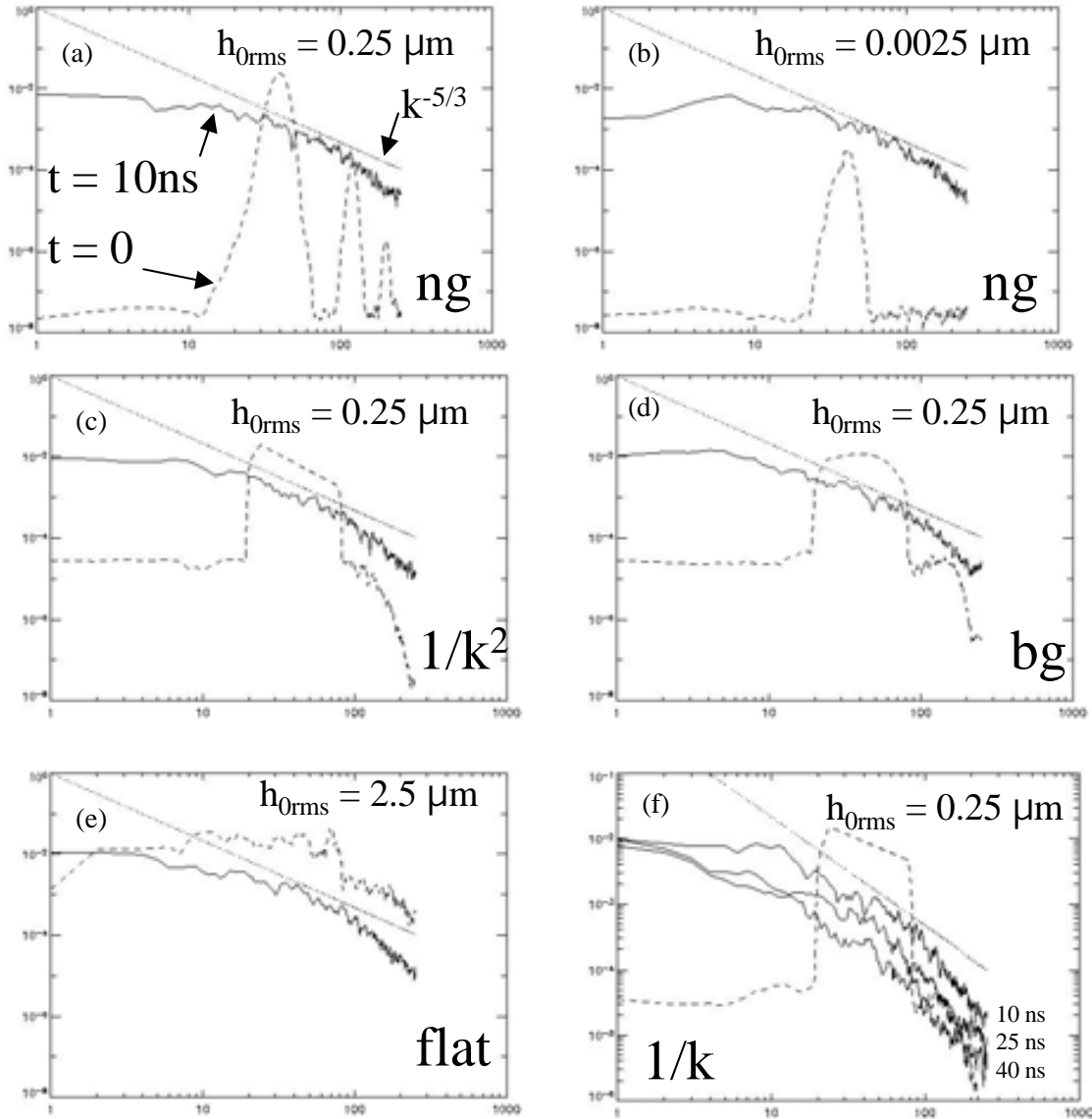


Figure 11: Loss of transverse spectral information. Density spectra at $t = 0$ and $t = 10$ ns for a variety of short-wavelength spectral shapes: (a) Narrow gaussian with $h_{0rms} = 0.25 \mu\text{m}$, (b) narrow gaussian with $h_{0rms} = 0.0025 \mu\text{m}$, (c) $1/k^2$ spectrum with $h_{0rms} = 0.25 \mu\text{m}$, (d) broad gaussian with $h_{0rms} = 0.25 \mu\text{m}$, and (e) flat (modes 4-80) with $h_{0rms} = 2.5 \mu\text{m}$. (f) hyperbolic ($1/k$) spectrum with $h_{0rms} = 0.25 \mu\text{m}$. By 10 ns, all transverse spectral information above about mode 10 has been lost, and memory of the initial conditions is retained only in the amplitudes of the long wavelength modes. For runs with the same initial rms-amplitude, the low-mode end of the spectrum is also very similar, suggesting that only memory of the initial amplitude and not the spectral shape has been retained. In (f), we include spectra at 25 and 40 ns. After establishment of the quasi-self-similar regime, there is little change in the spectra shape except for a steeper slope at the lowest modes.

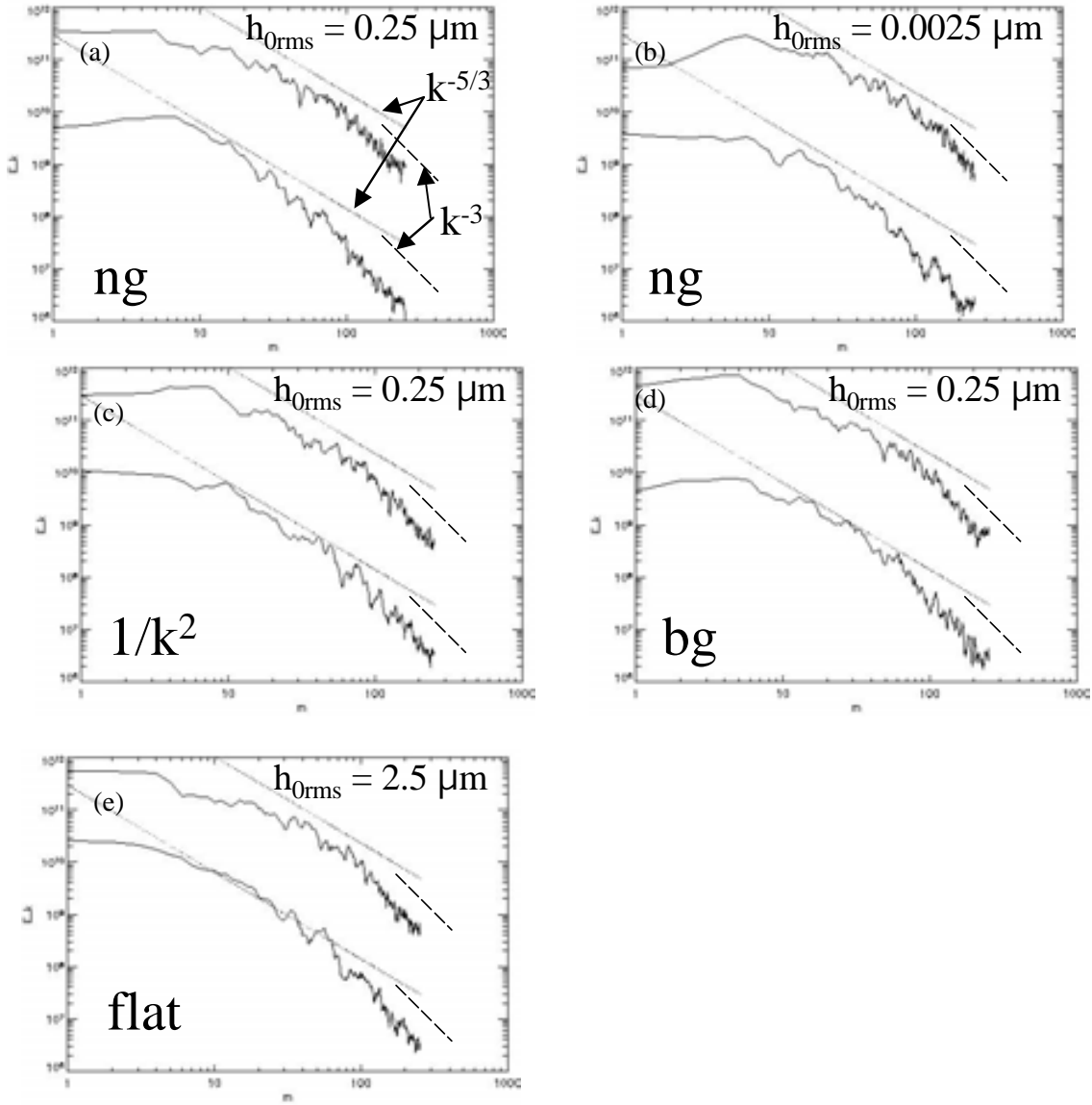


Figure 12: Transverse and parallel turbulent kinetic energy spectra at 10 ns. The upper solid curve is the parallel directed turbulent kinetic energy and the lower solid line is the transverse directed turbulent kinetic energy. (a) Narrow gaussian with $h_{0rms} = 0.25 \mu\text{m}$, (b) narrow gaussian with $h_{0rms} = 0.0025 \mu\text{m}$, (c) $1/k^2$ spectrum with $h_{0rms} = 0.25 \mu\text{m}$, (d) broad gaussian with $h_{0rms} = 0.25 \mu\text{m}$, and (e) flat (modes 4-80) with $h_{0rms} = 2.5 \mu\text{m}$. By 10 ns, the spectral shape depends weakly on the initial conditions, and both transverse and parallel components exhibit a limited $k^{-5/3}$ inertial range. In most cases, the high-mode end of the spectrum is reasonably well approximated by a $k^{-5/3}$ scaling consistent with a 2D forward enstrophy cascade.

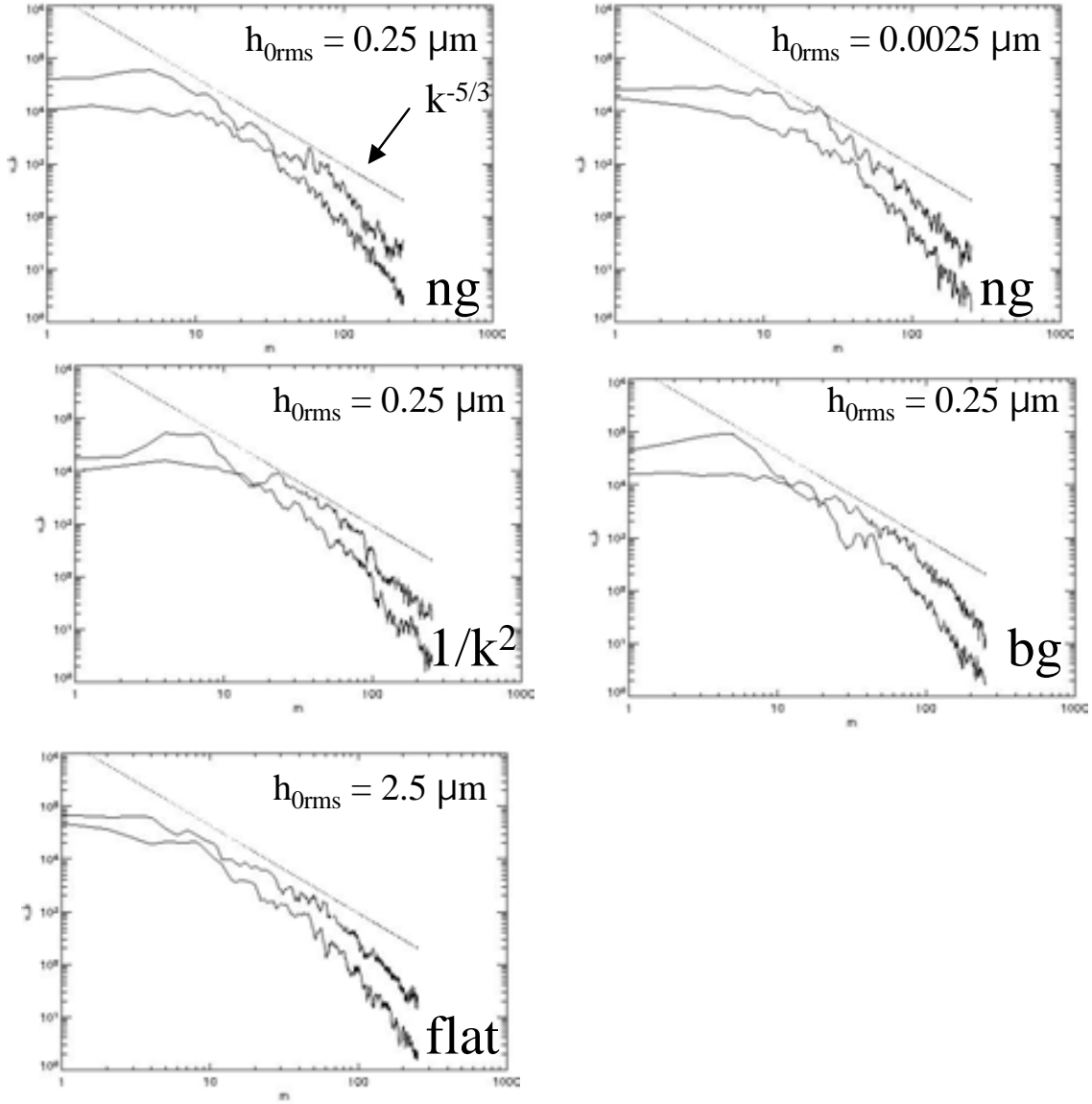


Figure 13: Transverse and parallel velocity fluctuation spectra at 10 ns. The upper solid curve is the parallel velocity fluctuation and the lower solid line is the transverse velocity fluctuation. (a) Narrow gaussian with $h_{0rms} = 0.25 \mu\text{m}$, (b) narrow gaussian with $h_{0rms} = 0.0025 \mu\text{m}$, (c) $1/k^2$ spectrum with $h_{0rms} = 0.25 \mu\text{m}$, (d) broad gaussian with $h_{0rms} = 0.25 \mu\text{m}$, and (e) flat (modes 4-80) with $h_{0rms} = 2.5 \mu\text{m}$. By 10 ns, the spectral shape depends weakly on the initial conditions, and both transverse and parallel components exhibit a limited $k^{-5/3}$ inertial range.

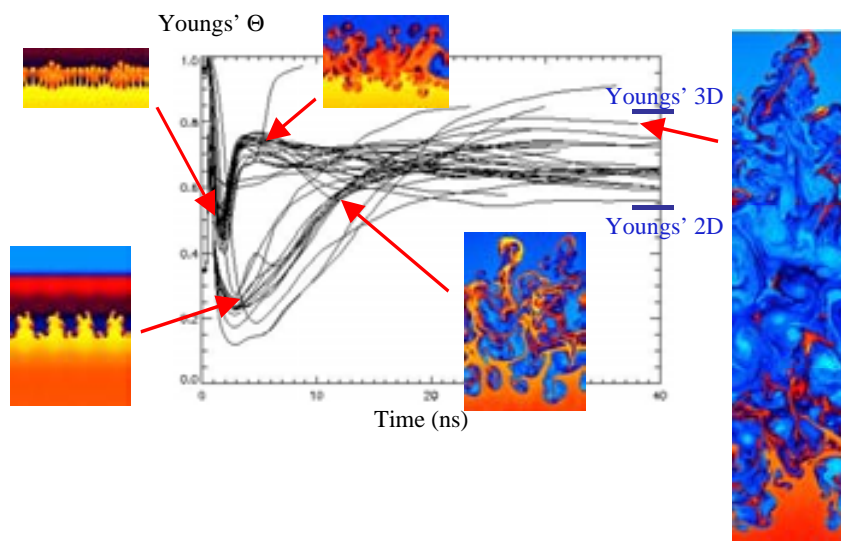


Figure 14: Degree of mixedness for all 52 2D simulations included in Fig. 5. Transition to quasi-self-similar regime results in an increase in mixedness. For a similar density ratio, Youngs* reports $\Theta \approx 0.83$ in 3D and $\Theta \approx 0.54$ in 2D [D.L. Youngs, Lasers and Particle Beams, 12(4), 725 (1994)].

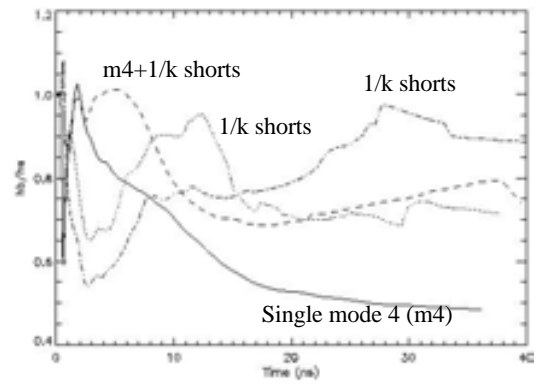


Figure 15: Bubble to spike amplitude ratio: In the single mode 4 case, the amplitude ratio approaches a value of about 0.48. This is just slightly higher than the value of 0.42 predicted by a buoyancy-drag model assuming that the spike reaches terminal velocity early on. With the spike interaction and breakdown associated with transition to the quasi-self-similar regime, the amplitude ratio is much closer to unity and typically greater than 0.7 at late times.

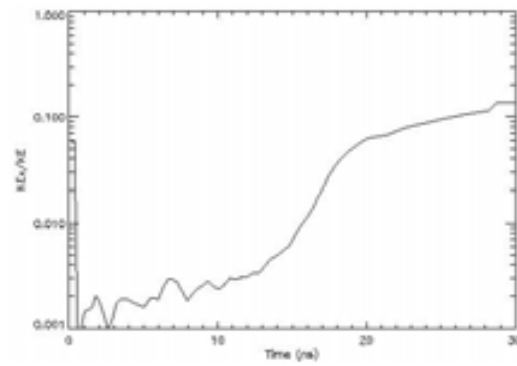


Figure 16: Ratio of transverse to total kinetic energy, integrated over the mix region, from the single mode 4 simulation. Below 15 ns, the relative transverse kinetic energy increases slowly. The breakup of the mode 4 spikes at 15-20 ns corresponds to a much faster order of magnitude increase.

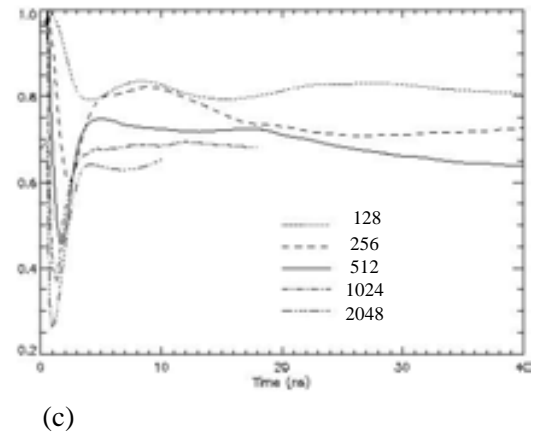
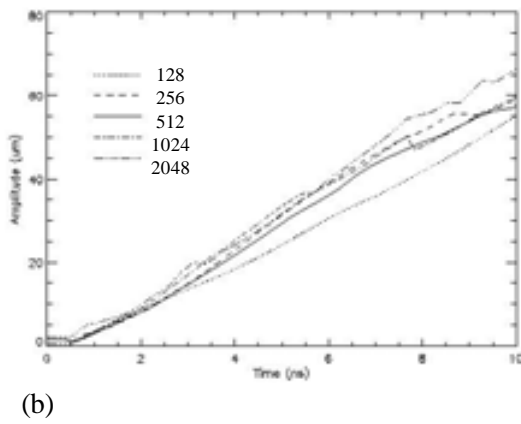
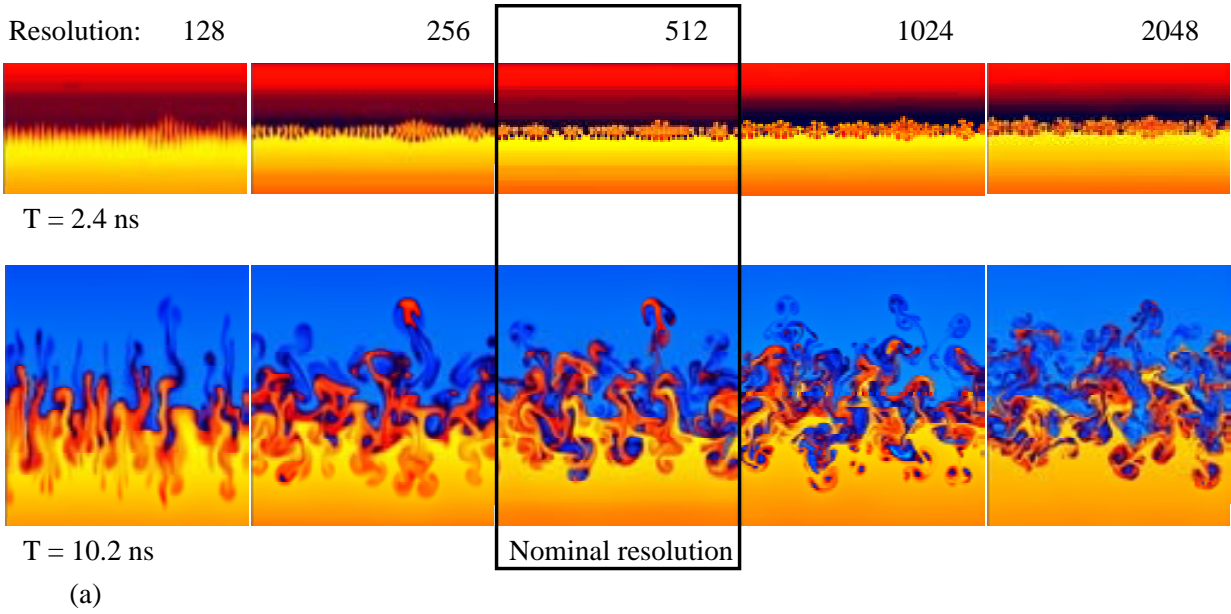


Figure 17: Resolution study: The resolution is varied from 128 to 2048 cells per box width (ppb), or from four times less than to four times greater than the nominal resolution of 512 ppb. (a) Log density plots and (b) perturbation amplitude histories suggest that the interface structure is reasonable well-resolved at 256 ppb. (c) A plot of the mixing parameter as a function of time shows that there is more mixing at lower resolution where the numerical diffusion is greater.

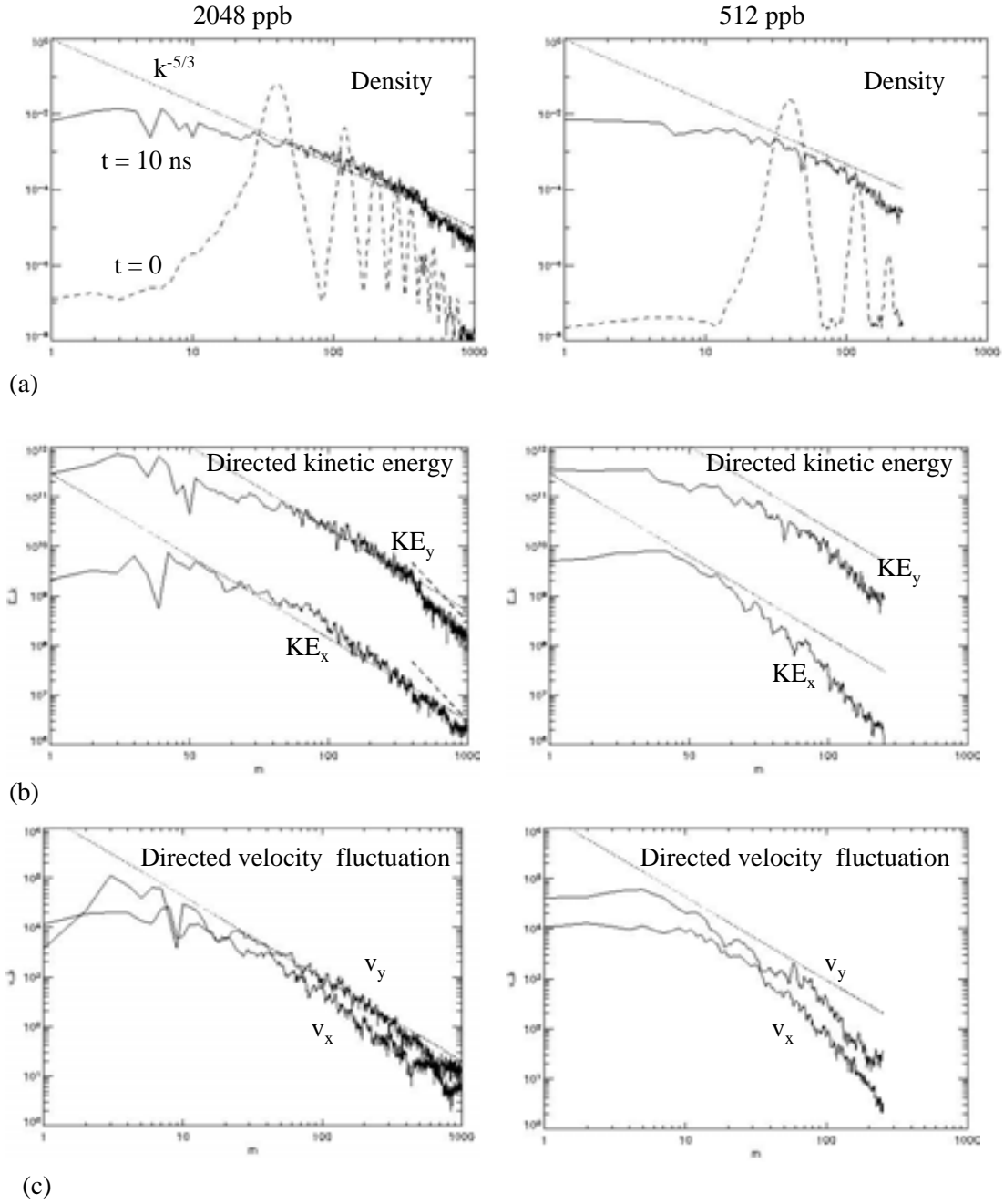


Figure 18: (a) Density, (b) directed turbulent kinetic energy, and (c) directed velocity fluctuation spectra at 0 and 10 ns for highest resolution (2048 ppb). The initial spectrum is narrow gaussian with randomized amplitudes and phases. Spectra from a 512 ppb case with the same spectral shape are included for comparison. In the energy spectra, dashed lines denote the k^{-3} scaling associated with a forward enstrophy cascade in 2D turbulence.

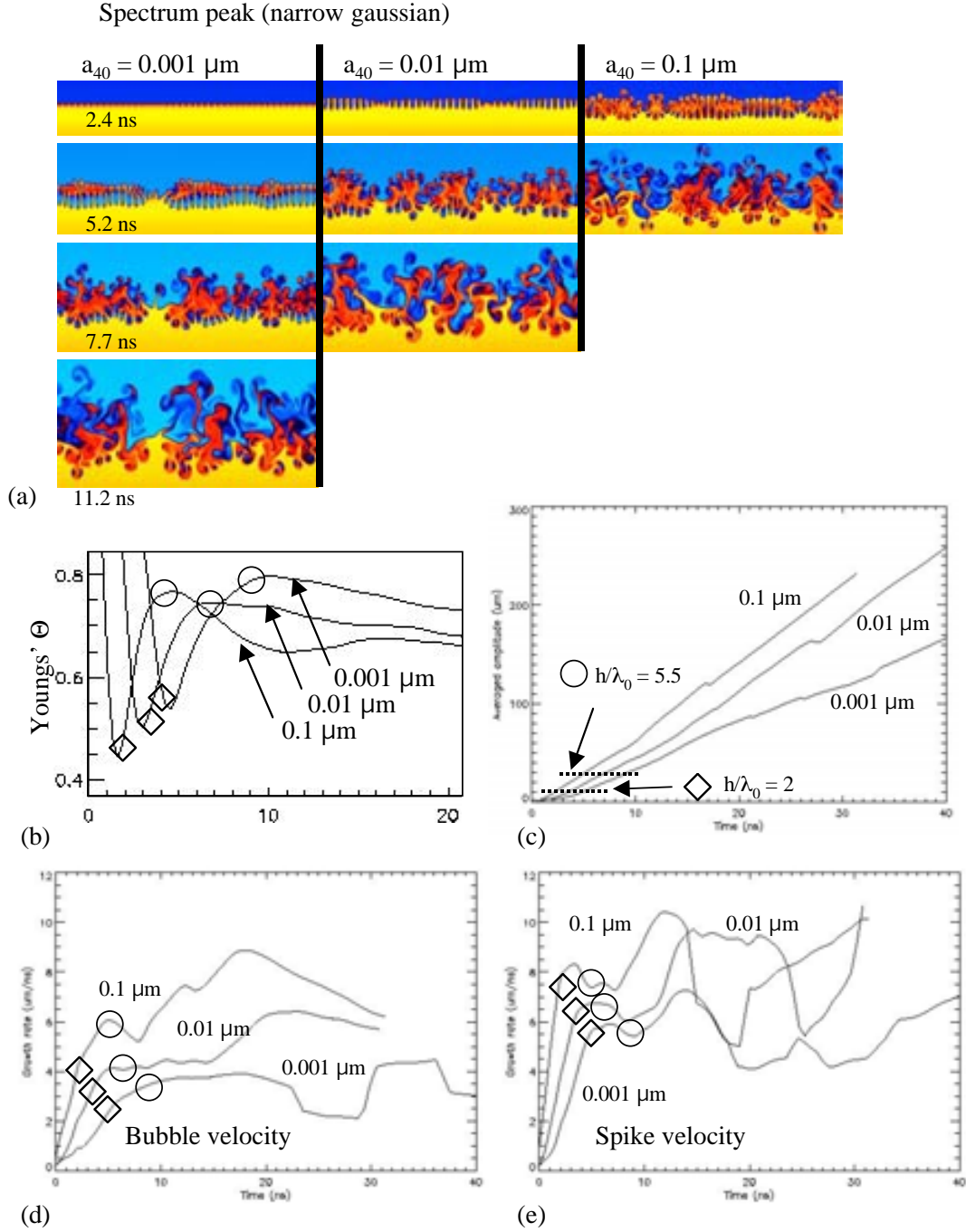
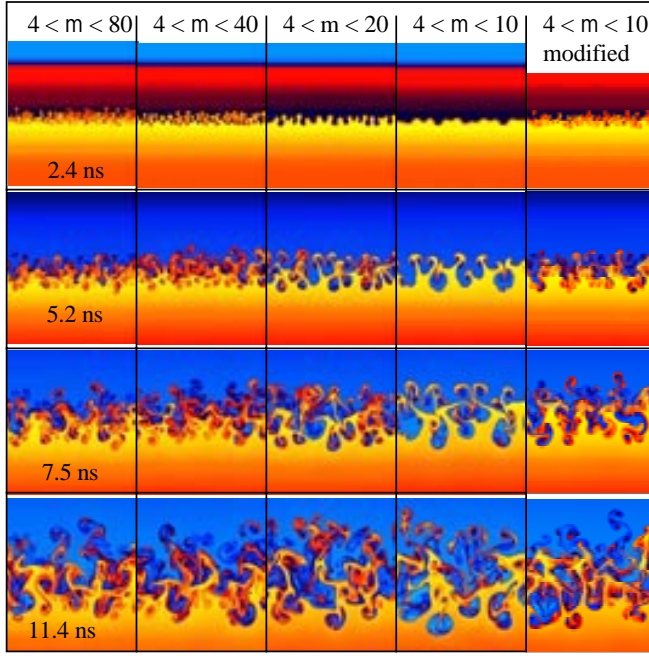
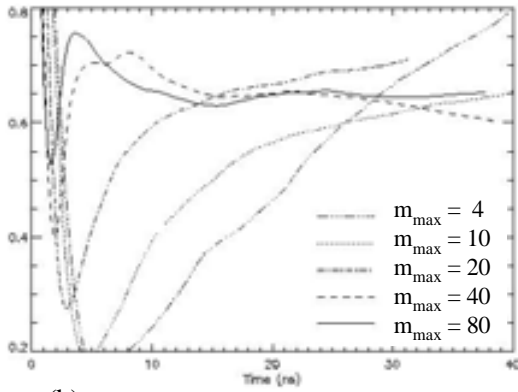


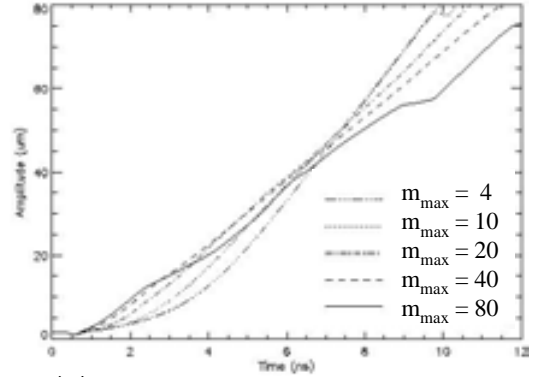
Figure 19: Dependence of amplitude growth and transition time on the initial rms-amplitude: (a) Log density plots show that spike interaction begins when $h/\lambda_0 \approx 2$. (b) The mixing parameter peaks at later times for smaller initial amplitude, coincident with the loss of initial transverse spectral information. (c) Amplitude histories show that the transition to the quasi-self-similar regime occurs when $h/\lambda_0 \approx 5-6$. (d) Bubble and (e) spike velocity histories show that spike breakup results in a reduction in the growth rate followed by accelerated growth after establishment of the quasi-self-similar regime and the generation of larger scales. In (b)-(e), the spike interaction threshold $h/\lambda_0 \approx 2$ is denoted by diamonds and the transition threshold $h/\lambda_0 \approx 5.5$ is denoted by circles.



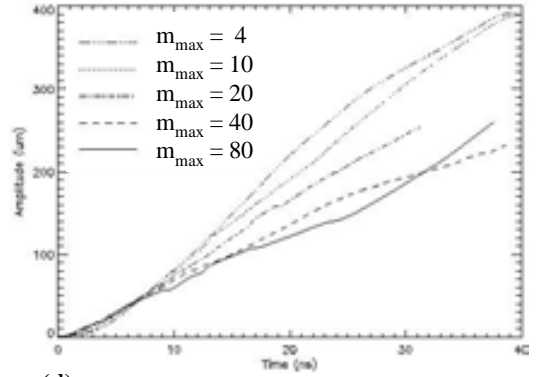
(a)



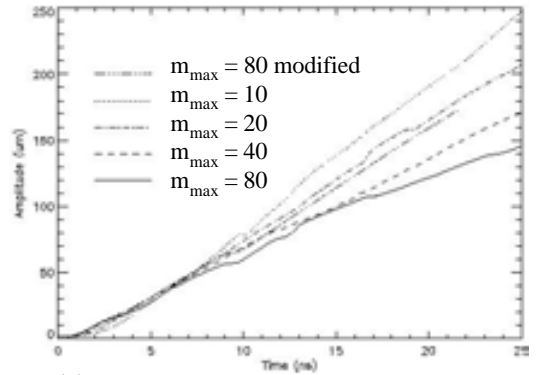
(b)



(c)

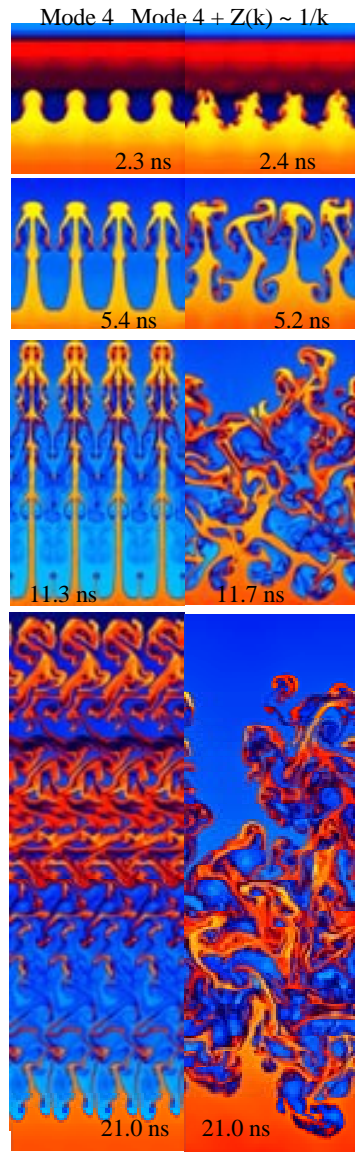


(d)

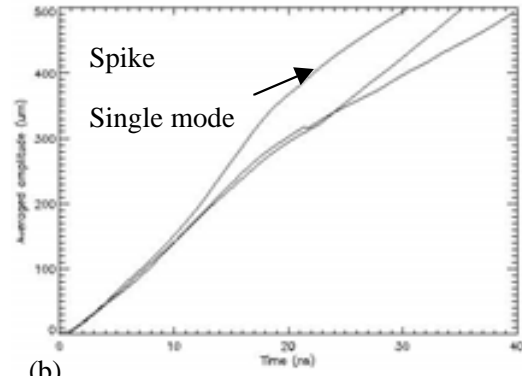


(e)

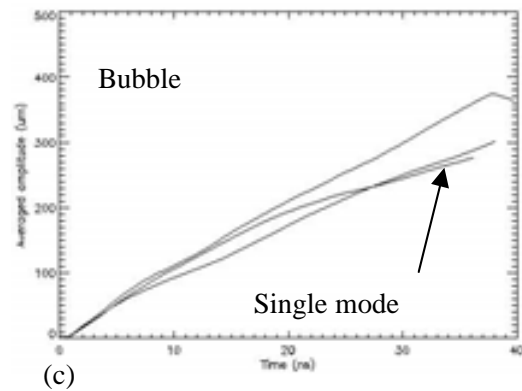
Figure 20: Variation of short-wavelength cutoff for flat spectrum from $m_{\max} = 4$ (single mode) to $m_{\max} = 80$. (a) Log density plots, (b) mixing parameter, and (c)-(d) amplitude histories show decreased mixing and enhanced growth with lower cutoff when the initial rms amplitude is fixed at $0.25 \mu\text{m}$. (e) A modified $m_{\max} = 80$ is constructed in which the the first 7 modes are replaced with the spectrum from the $m_{\max} = 10$ calculation. The initial rms amplitude is increased by nearly $\sqrt{2}$ relative to the $m_{\max} = 10$, but the amplitude is reduced to below the $m_{\max} = 20$ result.



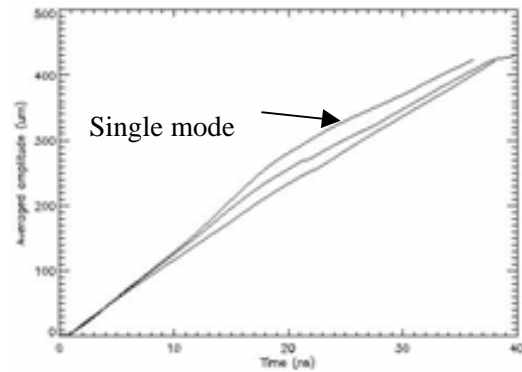
(a)



(b)



(c)



(d)

Figure 21: Effect of shorts on long: (a) Breaks the single-mode symmetry, resulting in (b) reduction in late-time spike growth and (b) enhancement of the late-time bubble velocity. (d) The net effect is an increase in the growth of the averaged amplitude. Amplitude plots include single mode 4, mode 4 with hyperbolic shorts, and mode 4 with broad gaussian shorts.

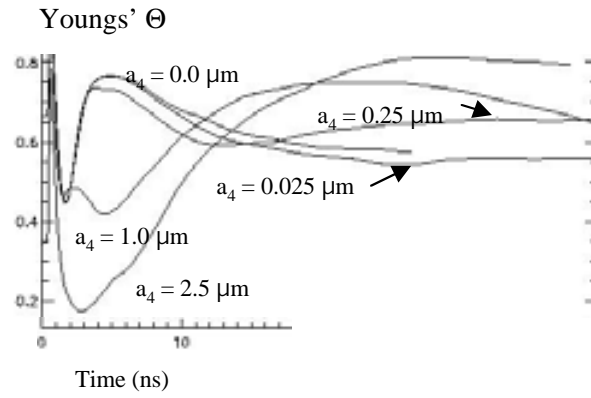
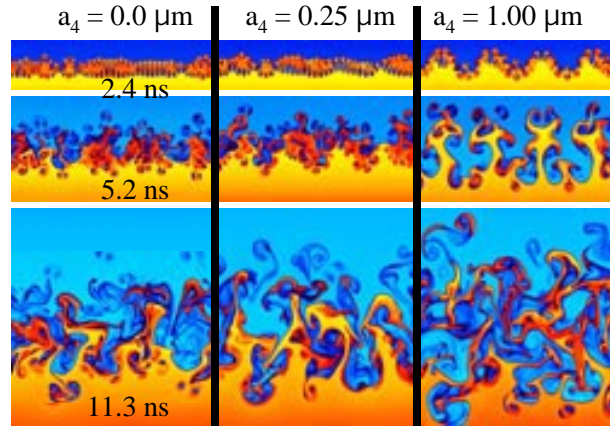


Figure 22: Effect of long on shorts. (a) Suppresses early-time growth of small-scale structure and (b) delays the transition to “turbulence”.